Time Dependence of Postseismic Creep Following Two Strike-Slip Earthquakes

Gerasimos Michalitsianos

29 April 2011, GEOL394

Thesis Advisor: Laurent Montési

Table of Contents

Figures

Tables

Tables (continued)

Abstract

The 28 September 2004 M_w 6.0 Parkfield and the 3 November 2002, M_w 7.9 Denali earthquakes each triggered postseismic deformation, a phenomenon commonly captured by geodetic data, including InSAR and GPS, in the aftermath of large earthquakes. Interpretations for postseismic deformation include viscoelastic relaxation, poroelastic rebound, or brittle aftershocks. The large magnitude difference between these two North-American strike-slip events leads us to question whether the rheological mechanism most responsible for the postseismic signature is the same between the two events. Here, I model geodetic time-series collected following both the Denali and Parkfield events, considering fourteen different possible postseismic displacement relations. A Levenberg-Marquardt inversion routine was used to fit these displacement functions through the time-series for the two events. A statistical method, the Partial F Test, was then used to compare these fits. The Partial F Test was ultimately unsuccessful because of noise in the GPS. Upon restricting the analysis to a study of one particular function, the General Relaxation Law with an added linear trend, a clear difference between the Denali and Parkfield datasets emerges. While the Denali postseismic dataset is best explained by Newtonian creep in a ductile shear zone with a larger degree of remote tectonic loading following a linear trend, the Parkfield dataset is best captured by brittle mechanisms supporting a rate-dependent friction with a relatively smaller linear trend. The mechanisms apparently associated with these earthquakes are compatible with my hypothesis that the Denali event, being larger than the Parkfield earthquake, activated deeper, ductile deformation mechanisms.

I. Introduction

The earthquake cycle may be partitioned into three different time intervals: a loading period, a coseismic (rupture) period, and a period of postseismic deformation (Montési, 2004). In this project, the focus was on postseismic signals recorded by Global Positioning System (GPS) stations. Mechanical explanations for this postseismic creep include brittle afterslip in the upper 15 km of the lithosphere, poroelastic rebound driving fluids in the upper crust, and viscoelastic relaxation confined to the lower crust and/or upper mantle (e.g. Bürgmann and Dresen, 2008). Afterslip is attributed to continued slip on the earthquake's original rupture area and viscoelastic relaxation is potentially localized deformation on a ductile shear zone in the upper mantle or lower crust (Marone *et al*., 1991; Montési, 2004). Peltzer *et al*. (1998) described poroelastic rebound as a change in the Poisson ratio (of transverse strain to axial strain) from unsaturated to saturated regimes with the dissipation of pore-pressure gradients following rupture events. This project aimed to compare the postseismic GPS relaxation signal following two North-American strike-slip earthquake events, namely the 3 November 2002 M_w 7.9 Denali Earthquake (63.5°N, 147.5°W) in south-central Alaska and the 28 September 2004 M_w 6.0 Parkfield earthquake (35.8°N, 120.4°W) along the San Andreas Fault (SAF) in southern California (see Fig. 1).

Figure 1: Locations of the Parkfield and Denali events. Both earthquakes occurred along strike-slip faults associated with the movement of the Pacific and North American Plates. The Denali fault ruptured with oblique convergence with the collision of the Yakutat terrain and stable North America, an intracontinental event strike-slip event; the Parkfield event occurred along the San Andreas Fault.

The rupture length of the Denali event was ~330 km, compared to a mere 23 km for that of Parkfield. The large magnitude difference between the Parkfield and Denali events corresponds to different possible origins of postseismic deformation (Freed *et al*., 2006a, b; Freed 2007; Johnson *et al*., 2006; 2009). This project evaluates to what extent the mechanisms most responsible for the captured postseismic signal are different between the two events. The Denali earthquake, being large than the Parkfield event, may have activated deeper deformation mechanisms, which give rise to different time dependencies of the postseismic deformation. Postseismic deformation following the Parkfield and Denali events has already been modeled on an individual basis in many publications with varying assumptions and techniques, giving implications for mechanisms behind postseismic deformation. Most studies used advanced numerical modeling from which only very specific questions could be asked. This project uses the *same* analysis to compare postseismic deformation following both events. Although the chosen inversion routine could not constrain where postseismic deformation actually occurs, it uses an analytical formula for the time dependence of postseismic creep and it can capture a wide range of rheological behaviors (Montési, 2004).The M_w 7.9 Denali earthquake was the largest strike-slip event in North America since the 1906 San Francisco event (Eberhart-Phillips *et al*. 2003). Freed *et al*., (2006a, b) used 3-D Finite Elements method to show that the Denali postseismic signal requires a power law rheology, implying strong variation in viscosity at depth, as a single linear rheology cannot fit initial GPS displacements (Figure 2).

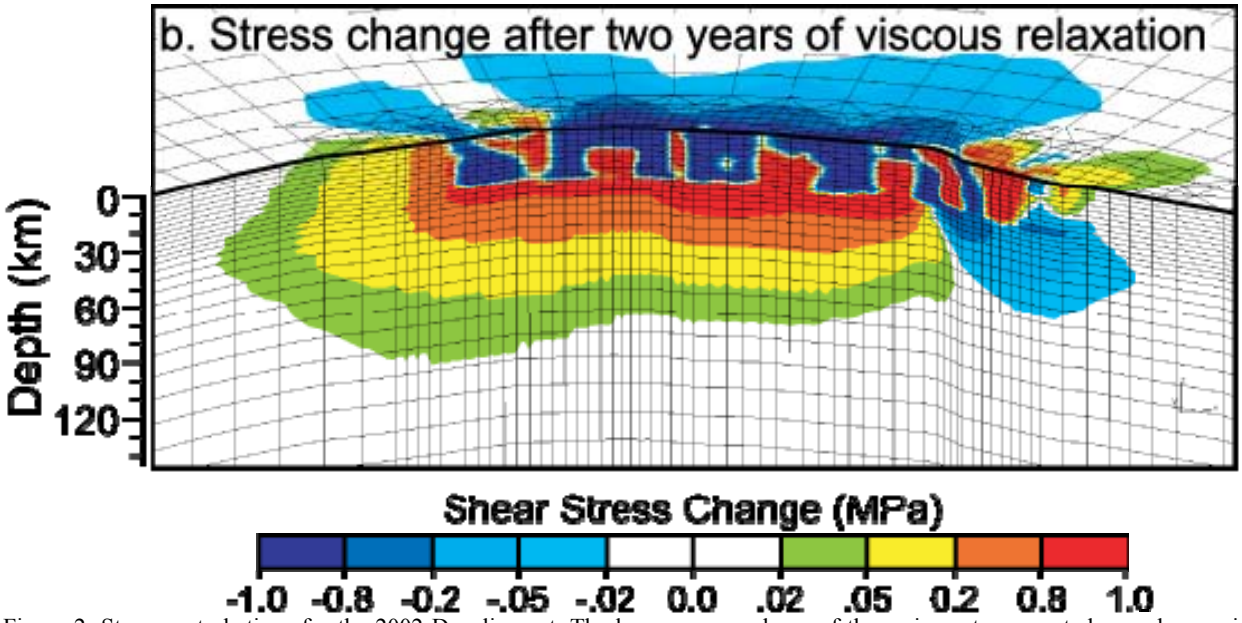

Figure 2: Stress perturbations for the 2002 Denali event. The huge energy release of the main rupture event shows changes in shear stress as deep as ~100km, below the crust-mantle boundary (Freed *et al.*, 2006), where deformation is more likely brittle than ductile.

Johnson *et al*. (2009) however, successfully fitted GPS time-series with a model combining Denali afterslip on a fault zone, which was ignored by Freed *et al*. (2006a, b), with distributed creep in a linear viscoelastic deeper layer in the lower crust and upper mantle (Figure 3).

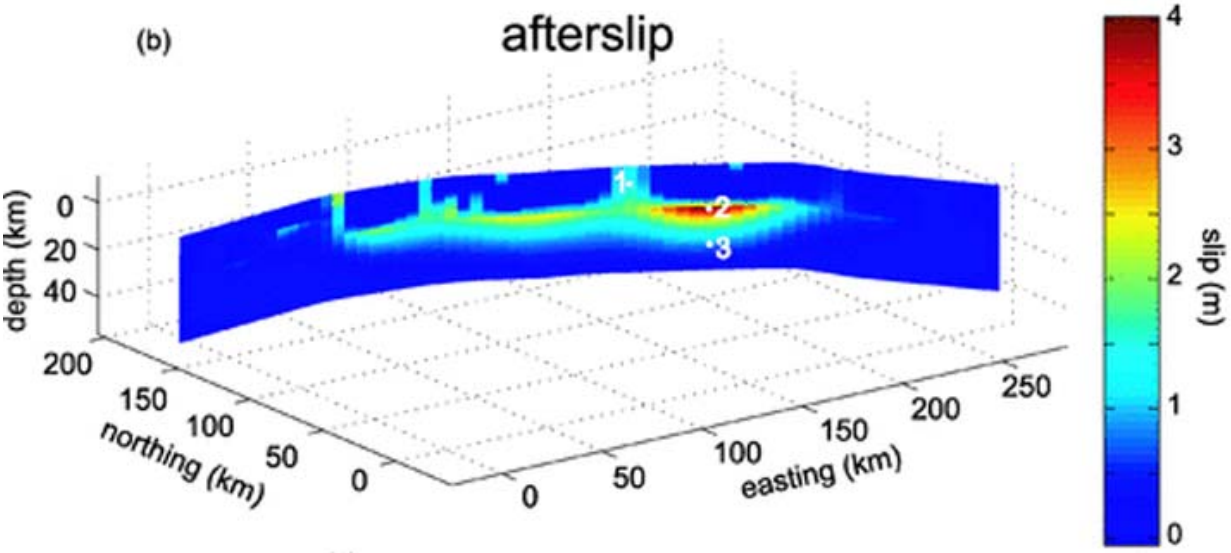

Figure 3: Slip extending as far deep as the mantle, ~90 km, following the 2002 Denali event (Johnson *et al*., 2009)

No single linear rheology could fit initial GPS displacements for the 2002 Denali event, as there was strong variation in lateral viscosity at depth, most likely represented by some non-linear flow law, with no need for afterslip. On the other hand, their technique cannot address non-linear distributed flow. Savage *et al*. (2005) captured the trend of postseismic deformation using a description of GPS time-series that assumes only a transient creep rheology but with a lack of spatial information. They did not test alternative rheologies. These studies agree that postseismic deformation after the Denali event is due to

several deformation mechanisms, including afterslip, possibly non-linear viscoelastic relaxation, and poroelastic rebound (Freed *et al*., 2006a).

In contrast to the Denali event, the 2004 Parkfield earthquake is the smallest magnitude event for which postseismic deformation has been recorded (Langbein *et al*., 2006). The 2004 Parkfield event is the latest in a sequence of earthquakes that has lasted over the last century, occurring at unusually regular intervals of roughly 20-25 years between earthquakes, with ruptures in 1934 and 1966. Therefore, the 2004 Parkfield event occurred in an extremely well instrumented area of the SAF with dense networks of GPS. The Parkfield event displayed a surprisingly intense postseismic signal of deformation: like the 1994 Sanriku earthquake, the energy release of postseismic deformation exceeded the energy release of the main rupture itself (Helmstetter and Shaw, 2008). Savage *et al*. (2005) suggested that the Parkfield signature, like the Denali signal, can be modeled with a logarithmic time dependence associated with a transient creep. However, 3D Finite Element models indicate that, unlike Denali, the postseismic deformation for the smaller Parkfield event appears to be limited to shallow afterslip, probably because the energy released in this event was not large enough to activate viscoelastic creep deep in the crust or poroelastic rebound (Freed *et al*., 2007) (Figure 4):

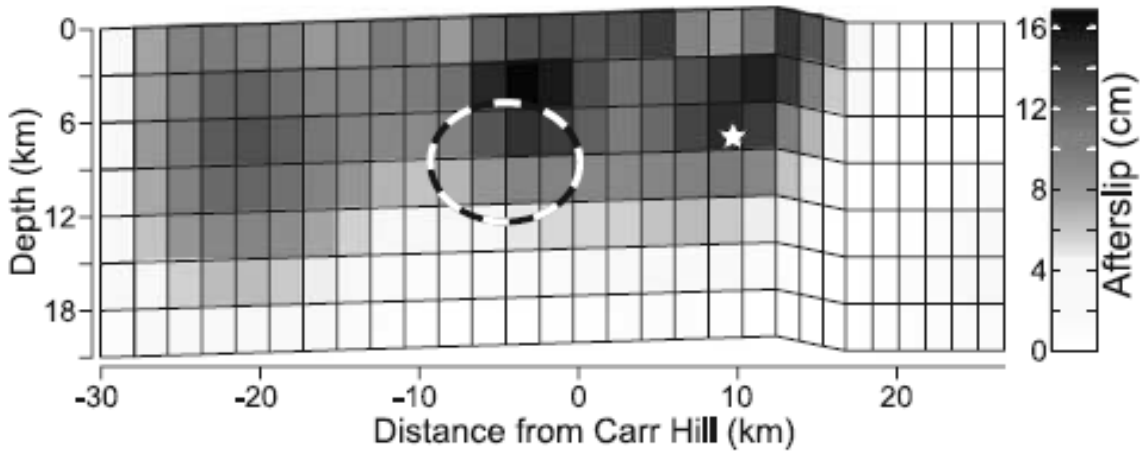

Figure 4: Afterslip associated with the 2004 Parkfield event; the smaller energy release of the rupture activated stresses confined to only the upper 15-20 km of the crust, which dominates the postseismic signal of the Parkfield event. The star denotes of the hypocenter of the Parkfield event, while the circle, where the circle indicates the greatest coseismic slip. (Freed *et al.* 2007).

Likewise, Johnson *et al*. (2006) successfully modeled GPS time-series using only brittle afterslip processes (Figure 5). Fig. 5 shows that for the Parkfield event, the signal of postseismic deformation was limited only to shallow brittle afterslip in the upper 15 km of the crust.

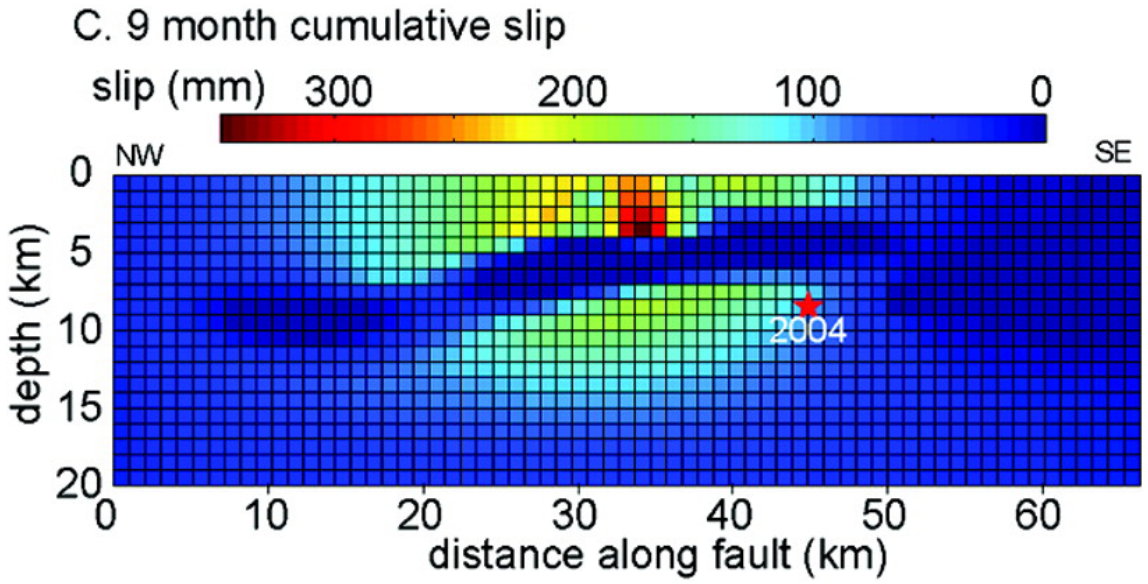

Figure 5: Afterslip for Parkfield, confined mostly to the upper 15-20 km of the lithosphere following the Parkfield event (Johnson *et al.*, 2006).

Although these studies all use different assumptions and modeling techniques and each consider only a limited number of physical processes, it seems most likely that postseismic deformation for the Denali event can be attributed to several mechanisms with a clear contribution of deep creep processes, while postseismic deformation following the Parkfield event can be explained solely using brittle afterslip. These studies used mainly the direction and magnitude of postseismic displacement but not the details of their time dependence. However, the rheologies used in these models are expected to produce different time dependences of postseismic creep (Montési, 2004). Therefore, I analyzed GPS time-series collected after the Denali and Parkfield events to determine if we can resolve a difference in their time dependences. This problem is important in that we can learn more about the dynamics of the deforming lithosphere in both south-central AK and in southern California. Implications carry over into a better understanding of the earthquake cycle and prediction, which may also have major societal significance for Americans in CA and AK.

II. Overview

This study aims to determine what mechanism is responsible for the postseismic creep produced by the 2002 Denali and 2004 Parkfield earthquake events. Possible mechanisms include poroelastic rebound, viscoelastic relaxation in the lower crust or upper mantle, or brittle shallow afterslip confined to the upper 15-20 km of the crust. My hypothesis was that the time dependencies of postseismic creep imply different rheologies for the Denali and Parkfield events. This hypothesis is based from the previous research by Freed *et al*. (2006a, b. 2007) and Johnson *et al.* (2006, 2009). Two tests of this hypothesis were devised. In the first, we consided fourteen proposed time dependencies for postseismic creep, many of which are associated with a specific rheology. I attempted to determine statistically which of these is most appropriate for each GPS time-series using a Partial F Test. However, this test proved too sensitive to noise in the data for any meaningful conclusions to be made. Though this attempt to compare all fourteen displacement functions between two very different major North-American events was unsuccessful, this work was an important first step toward developing a successful strategy to compare all displacement functions. It is the first attempt to consider all fourteen displacement relations and compare them between two earthquakes.

The second test was to select one function in particular: the General Relaxation Law (GRL) with an added linear trend (GRL + L). One parameter of this relation, the stress exponent ξ, characterizes the type of rheology used to predict the time dependence of postseismic deformation. I show that the Parkfield dataset implies $\xi \sim 0$, which is characteristic of brittle creep, whereas the Denali dataset implies $\xi \sim 1$, characteristic of Newtonian creep. Hence, I was able to document a fundamental difference in the deformation mechanism used to explain postseismic deformation in these two events. This result supports my hypothesis that postseismic deformation from the Parkfield event is generated as shallower depth in the crust, where deformation is brittle, compared to the Denali event, where deformation is ductile.

III. Background of the Displacement Relations, & Analysis of Uncertainty

Fourteen different mathematical laws as displacement functions of time have been proposed to represent the time-dependence of the postseismic GPS signals (see Table 1 in Appendix A). Each of these is associated with a particular rheology and mechanism responsible for postseismic creep. These fourteen relations contained between two and five parameters that were determined using Levenberg-Marquardt (LM) inversion routine. Some of these parameters have actual physical meaning (i.e. initial velocity on fault plane after rupture, initial displacements, or time constants). Others describe the shape of the time dependence function and may be related to the underlying rheological laws. For example, ξ in the General Relaxation Law may correspond to the inverse of the stress exponent of a power law relationship, if $0 < \xi \leq 1$.Some of these laws were also formulated by taking one fundamental relation that is linked to a rheology-motivated time dependence and adding a linear trend (and hence, one more parameter). The linear trend represents processes not associated with postseismic creep, like large-scale plate motions or residual signals from other nearby earthquakes.

It is expected that, the more parameters in the relation, the better fit to the GPS time-series. Before rheological interpretations can be done concerning the physical origin of each of the displacement relations, it is important to determine how many parameters can be constrained with the available data and rank the relative success of all fourteen possible time dependencies for the various GPS stations. I attempted to determine this ranking using a Partial F Test and a constructed hierarchy that links the fourteen mathematical relations for possible time dependencies of postseismic deformation (Fig. 6).

In this project, datasets were accessed through the website of the USGS. Links to the time-series are provided below Table 1 in Appendix A. The downloaded datasets contained uncertainty estimates for every GPS data point. The Levenberg-Marquardt inversion routine provides a covariance matrix that is used to estimate a formal uncertainty. However, the uncertainty reported here neglects coupling between different fit parameters and is therefore a minimum estimate to the actual parameter uncertainty. The Levenberg-Marquardt inversion routine is described in Appendix B. During the spring 2010 semester, data tables containing fit parameters and χ^2 values were collected for the Parkfield event.

A Partial F Test statistical analysis using the residual χ^2 of each fit was implemented to evaluate rigorously which formulation of postseismic creep best captured observations for the Parkfield event. During the spring 2011 semester, the same was done for the Denali event and a comparison was attempted. A study of synthetic time-series was also conducted to evaluate the accuracy of the technique. In the next section, I will give a brief overview of each of these laws, their origin based on past research, and how they were applied to mechanisms responsible for postseismic creep. I will also review how these fourteen different relations related to one another, presenting a hierarchy map that represented how I attempted to compare the fourteen different fits.

IV. Overview of Fourteen Displacement Relations & their Hierarchy

The most general relations used in this work is the General Relaxation Law (GRL), with an added linear trend (GRL+L), given by equation (1):

$$D_S(t) = D_0 + \frac{V_0 \tau}{\xi}\left(1 - \left(1 + (1-\xi)\frac{t}{\tau}\right)^{\frac{1}{1-1/\xi}}\right) + v_L t \tag{1}$$

where D_s is the displacement (mm) as function of time t in years, D_0 is the initial displacement, and V_0 the initial velocity. The parameter defining the shear zone rheology ξ describes the shape of the displacement relation (Montési, 2004). The original GRL relation was derived for power law creep in a ductile shear zone rheology and applied to the 1994 Sanriku and 2001 Peru events by Montési (2004). The GRL arises from the solution of an ordinary differential equation that links a spring representing the elastic lithosphere and deforming region with a power law rheology. The stress exponent n of the shear zone rheology is related to ξ according to $\xi = 1/n$. Adjusting the value of ξ is equivalent to changing the rheology of the shear zone from Newtonian creep ($n = \xi = 1$) to brittle creep ($\xi = 0$). Note that ξ could have negative values, which may reflect the presence of a long term steady motion of the GPS station that is not related to the shear zone rheology (Montési, 2004).

In (1), V_0 is a deforming shear zone velocity and D_0 (an integration constant) is the initial displacement of the shear zone immediately following the main rupture event in the beginning of the postseismic time interval for time $t = 0$. Also in (1), τ is a time constant defined as the ratio of the shear zone velocity to the shear zone acceleration at a time $t = 0$ with $v_L = 0$. In the special case $\xi = 1$ (Newtonian rheology), Eq. 1 simplifies to a well-known exponential relaxation (Equation 2**):**

$$D_s(t) = a + b\exp\left(\frac{t}{\tau}\right) \tag{2}$$

Dislocation creep is thought to be active in many rocks in the lower crust and upper mantle. It is often described by a power law rheology with $n = 3$ or $n = 5$. We consider as a separate relation, the power law relaxation, with the special case ξ=1/3 of Eq. 1 that corresponds to dislocation creep (Eq. 3):

$$D_S(t) = D_0 + 3V_0\tau\left(1 - \left(1 + \frac{2t}{3\tau}\right)^{3/2}\right) \tag{3}$$

Brittle faults at low pressure and temperature may exhibit postseismic deformation if they obey velocity strengthening frictional sliding, in which case postseismic deformation is described by Eq. 4 (Marone *et al*., 1991):

$$D_S(t) = D_0 + V_0 \tau \log\left(1 + \frac{t}{\tau}\right) \tag{4}$$

Eq. 4 is formally equivalent to Eq. 1 with ξ = 0 (Montési, 2004). It is also occasionally called the Lomnitz law (Savage et al, 2008). A linear trend v_L may be added these laws for a better fit to the GPS time-series, and create four new possible relations with one more parameter each. One more possible that law that was considered in this project is given by (5). It is called the Modified Omori Law, and was originally proposed to explain the decay rate of aftershock sequences.

$$D_S(t) = a + b[1 - (1 + \alpha t)]^{1-p} \tag{5}$$

It is mathematically similar to the GRL if $p = 1 / (1 - \xi)$ (Savage et al., 2008), but gives a different parameterization, which may result in different fits if an iterative inversion relation is used. We also considered the case of a Modified Omori law with an added linear trend. The displacement function (6) is called the Burgers relation and it implies a Burgers body rheology.

$$D_S(t) = a + b_1 \exp(-\alpha_1 t) + b_2(-\alpha_2 t) \tag{6}$$

The Burgers body rheology consists of a Maxwell fluid (with immediate elastic response, ultimate Newtonian fluid behavior) and a Kelvin body assembled in series (Hetland and Hager, 2006). We refrain from adding a linear trend to Eq. (6) because this would result in a 6-parameter displacement relation. According to Bürgmann and Dresen (2008), the Burgers Body Law can represent the postseismic responses defined with two relaxation times, which might occur in the lithosphere undergoing transient creep or a nonlinear flow law with weak inclusions (Bürgmann and Dresen, 2008).

Savage *et al*. (2006) used a logarithmic trend to model postseismic creep following several earthquakes, including the 2003 San Simeon and 2004 Parkfield earthquakes (Equation 7),

$$D_S(t) = a + b \log(t) \tag{7}$$

where *a* (mm) and *b* (mm/yr) are constants to give a best fit and have little physical meaning. We may add the usual linear trend to the logarithmic trend to obtain another relation. Finally, we consider a simple linear trend (Equation 8),

$$D_S(t) = a + bt \tag{8}$$

that represents the unlikely null hypothesis for which no transient postseismic creep can identified. Linear trends are assumed only to result from remote plate motion or possible postseismic creep from residual motion from other, earlier nearby earthquakes. For example, postseismic GPS displacements from the 2003 San Simeon earthquake, whose epicenter was only 50 km from Parkfield, may affect the Parkfield postseismic time-series (Savage *et al*., 2005). The fourteen possible relations are summarized in Table 1 (Appendix A), which also indicates the number of parameters in each relation and provides references to previous studies that used each relation.

V. Hierarchy of the Fourteen Displacement Functions

The fourteen different proposed displacement functions of time are all mathematically interconnected. Based on the numbers of parameters each relation contains and what rheologies are implied (and hence what mechanism is implied to produce postseismic signals), we created a hierarchy and grouped these fourteen relations. The purpose of this hierarchy was to determine which laws are actually meaningful to compare relative to one another. For example, for a first grouping of these relations, notice that the GRL relation with an added linear trend becomes the standard GRL relation when $v_L \to 0$. The regular GRL (four parameters) relation then became the regular Lomnitz, Power, and Exponential relations (with three parameters) when $\xi \to 0$, $\xi \to 1/3$, $\xi \to 1$, respectively. The regular Lomnitz, Power, and Exponential relations can also be obtained by removing their linear trends letting $v_L \to 0$. In addition, the GRL Linear relation (five parameters) becomes the Lomnitz, Power, and Exponential relations (with linear trends, each four parameters) when we let $\xi \to 0$, $\xi \to 1/3$, and $\xi \to 1$, respectively. The example just given can be considered as one grouping, where the GRL, Power, Exponential, and Lomnitz laws (all with or without linear trends) were all be related to one another by adjusting numbers of parameters.

As another example, consider the Burgers Law (five parameters) given by (6). This relation is the sum of two exponential functions of time, each of which can be represented by the Exponential Law (2). Also consider second logarithmic relation with a linear trend, which further decomposes into both the linear trend and the logarithmic trend when we let $v_L \to 0$. Third, consider again the Modified Omori Law given by (5). The Modified Omori Law becomes the Modified Omori Law with a linear trend by adding $v_L t$. By setting parameter values of more complex laws to fixed values; we can recover a simpler relation with fewer parameters. All the laws will eventually simplify to a logarithmic or linear trend.

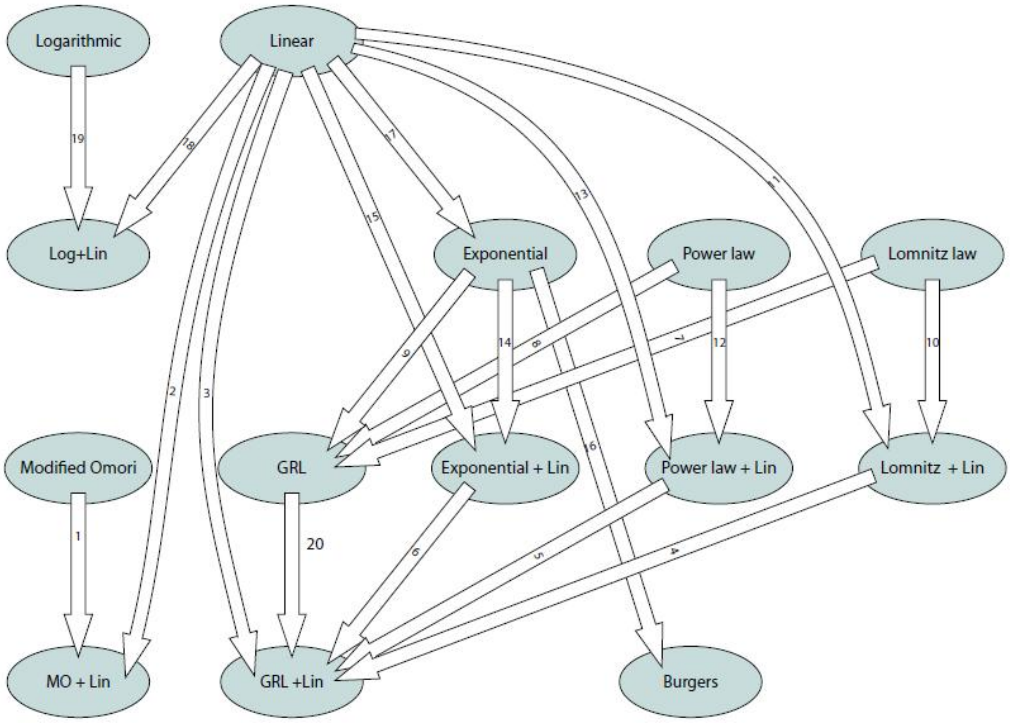

Figure 6: Hierarchy relating 14 possible time-dependencies of postseismic creep. The fourteen possible laws are organized into five stories corresponding to the number of parameters they contain. There are 20 links connecting the various laws. The numbers in each of the arrows were merely used for indexing purposes, and have no physical meaning here.

We summarize all these relationships among our fourteen functions in Fig. 6. The figure is essentially a map, analogous to a five-story building, where each successively higher level going up contains one more parameter, varying between two and five. There are twenty links. More parameters should make for a better fit to the displacement time-series, as quantified by a reduced χ^2. However, the improvement may not be statistically significant: the reduction in χ^2 might have only been achieved by fitting better noise in the dataset set rather than any actual physical motion. Thus, we need a statistical analysis to determine if the reduction of χ^2 is significant compared to the increase number of parameters along each link of Fig. 6. The Partial F Test was designed to conduct such analysis, but it proved to be too sensitive to noise in the real GPS datasets to provide meaningful conclusions.

VI. The Partial F Test

The Partial F is intended to be an an estimate of the probability that the improvement in quality of fit when following one the arrows in Figure 6 is not due to a random process (and therefore meaningful from a physical standpoint). Let χ_1^2 denote the goodness of fit for a relation with N_1 fitting parameters and χ_2^2 denote the goodness of fit for another relation containing N_2 fitting parameters, where both relations are linked together somewhere in Fig. 6. Also, let *n* be the number of displacement data points in a particular GPS time-series. The fit improvement *F* is given by Equation 9:

$$F = \frac{\chi_1^2 - \chi_2^2}{\chi_1^2} \frac{n - N_2}{N_2 - N_1} \tag{9}$$

Then we compute the probability α that F is not due to a random process using the F cumulative distribution function fcdf in MATLAB. For each GPS station, twenty partial *F* values were produced (for the 20 links in Fig. 6), and for each partial *F* value, an α value was computed using MATLAB's pre-programmed cumulative distribution function. When $\alpha > 0.95$, we are very confident that the link between the relations is valid, and hence we are justified to use the relation with more parameters to give a best fit to the postseismic time-series. When $\alpha < 0.90$, we are *not* confident that adding one more parameter to our displacement will yield a significantly better fit. If one relation (with *N* parameters) provides a significantly better goodness of fit than another relation (with *N* - 1), then we expect the α value to be very close to one.

We tried to further increase our confidence by conducting a bootstrap analysis of the original time-series, which was performed by using an increasing number of data points, *n*. First, the goodness of fits and α were used for some small value of *n* in equation (9), perhaps around a few hundred data points selected at random from the original dataset restricted in the postseismic interval. With only using a few data points, we expected that many of our α values will be much less than one, sometimes being close to zero. The Partial F Test was then performed again, this time using even more random data points in the time-series. By using successively more random data points, the bootstrap method covers the entire given time-series in the postseismic interval, yielding twenty Partial *F* and α values for each GPS time-series.

VII. Evaluation of the Partial F Test

As we conducted Partial F Test analyses on the Parkfield and Denali datasets, it proved difficult to reach a consistent conclusion. This motivated an evaluation exercise of this type of analysis using a synthetic dataset constructed in such a way that we know what the conclusion of the analysis should be; it was successful. A first synthetic time-series was constructed using the exponential relaxation law (Equation 2) and the total displacement (amplitude) of the MENT GPS station, which is just south of the main Denali fault. Tests were conducted with four noise realizations: 1) no noise (Fig. 7); 2) random noise only; 3) random walk only; 4) both random noise and random walk (Fig. 9).

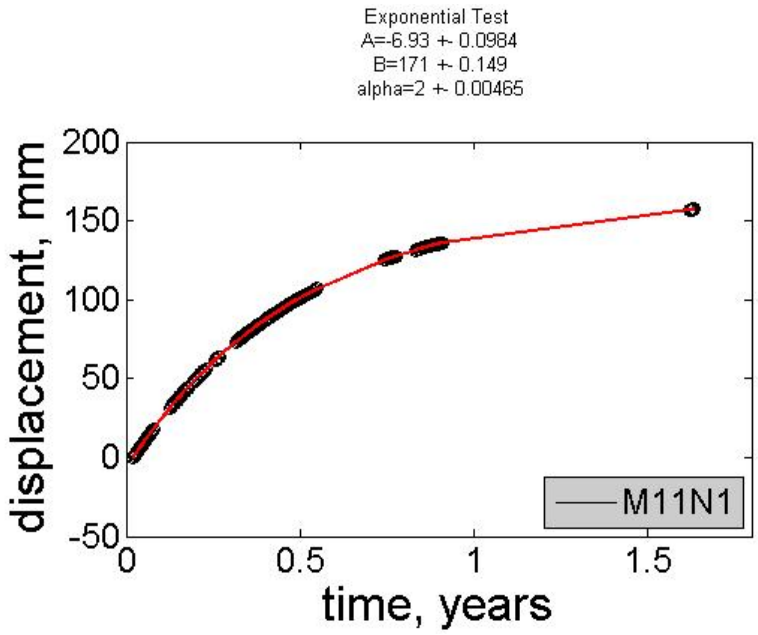

Figure 7: The Exponential relation fit through a MENT synthetic time-series with zero noise. The displayed fit parameters above the plot A, B, and alpha correspond to a (mm), b (no units), and α (1/mm), respectively, seen in Equation 2.

Table 1 shows the corresponding χ^2 values for all fourteen displacement functions fit through the zero-noise time-series of Figure 7. Note that the Exponential relation has the smallest χ^2 value of all the relations in Table 1. This is expected, as we know the time-series was created from Equation 2.

Table 1: χ^2 Values, Synthetic MENT, Random Walk and Zero Noise

Relation	χ^2	Relation	χ^2
Linear	1500	Exponential + Linear	0.040
Logarithmic	440	Modified Omori	0.098
Logarithmic + Linear	230	Power	28
Exponential	0.0045	Power + Linear	0.34
Lomnitz	61	Burgers	0.025
Lomnitz + Linear	0.56	Modified Omori + Linear	0.087
GRL	0.016	GRL + Linear	0.093

Table 1: Summary of the χ^2 values for the fourteen proposed time-dependencies of postseismic creep. These values were compiled for a synthetic time-series with zero noise. Notice that the Exponential relation has the smallest χ^2.

Figure 8 meanwhile shows a hierarchy created for the same time-series:

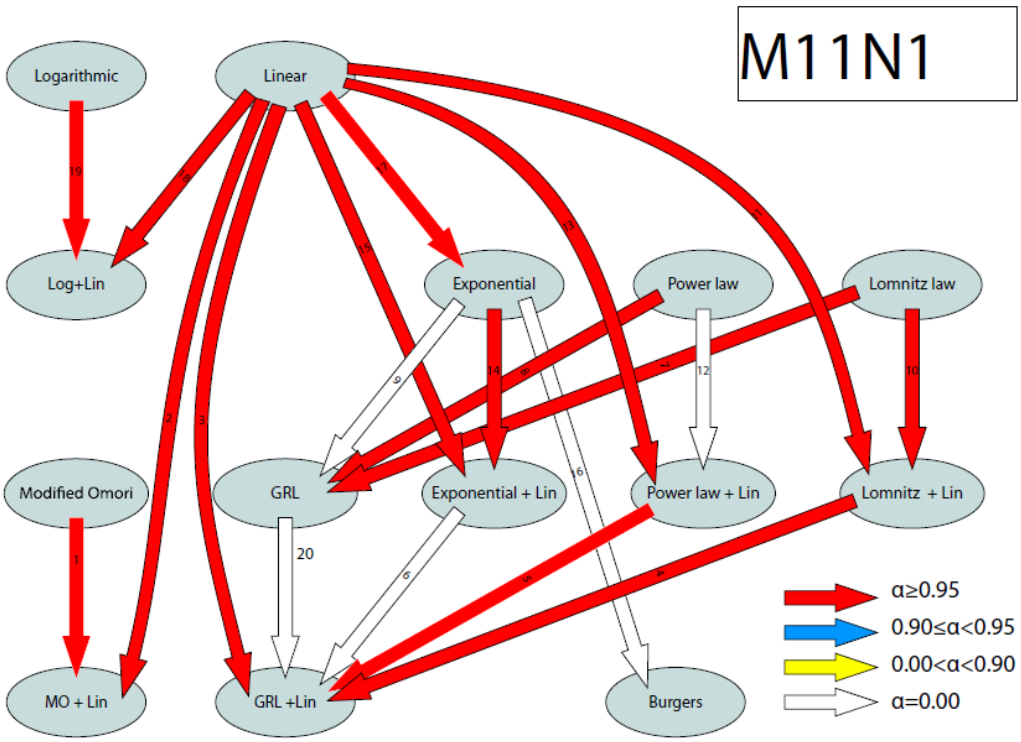

Figure 8: A hierarchy for a time-series with total displacement amplitude similar to the MENT time-series. Here the noise level is reduced to zero. This synthetic record was created using the Exponential relation (2). Red arrows indicate $\alpha \geq 0.95$, blue arrows indicate $0.90 \leq \alpha < 0.95$, yellow arrows indicate $0.00 < \alpha < 0.90$, and white arrows $\alpha = 0$. Here, the Exponential Law is the best fit, as explained above.

Red arrows indicate $\alpha \geq 0.95$, blue arrows indicate $0.90 \leq \alpha < 0.95$, yellow arrows indicate $0.00 < \alpha < 0.90$, and white arrows $\alpha = 0$. The hierarchy of Fig. 8 can be used to eliminate all but one of the fourteen relations. The linear and logarithmic trends at the bottom are eliminated as there are other relations (with more parameters) that yield a significantly better fit (as evidenced by the red arrows leading *away* from these). As the GRL relation does not yield a significantly better fit than the Exponential relation, GRL is eliminated. The GRL+L relation yields a significantly better fit than the Power and Lomnitz relations (with linear trends), yet the GRL+L relation does *not* yield a better fit than, say, the GRL relation (without the linear trend). This means that the GRL, Power, and Lomnitz relations (with linear trends) are eliminated from consideration as a best possible representation of the time-series. Also note that the Lomnitz relation with the linear trend yields a significantly better fit than the Lomnitz relation without the linear trend. This eliminates the latter. The Modified Omori is also eliminated with an improvement with adding the linear trend, while the Burgers relation is eliminated from the hierarchy as it cannot provide an improvement the Exponential relation.

Using the simplest remaining relations (Exp, Exp + L, and Lomnitz + L); we can compare their χ^2 values to see that the Exponential relation, with*out* the linear trend, is the best fit to the time-series (see Table 1). This validates the approach of using a partial *F* test analysis, as the Exponential relation was used to create the synthetic time-series in the first place. While this method had its flaws, including not being able to compare relations (with connecting arrows) with the *same* number of parameters, just as

well as some relations having no arrows leading *to* them (i.e. Lomnitz), it was still able to narrow down the possible candidates to just a few of the relations.

A more realistic time-series would include noise, both normal noise and random walk. In the real GPS time-series, the random and normal noise may have been due to seasonal variations in the time-series (i.e. groundwater movements). Figure 9 shows the Exponential relation fit through a MENT synthetic time-series with normal and random-walk noise.

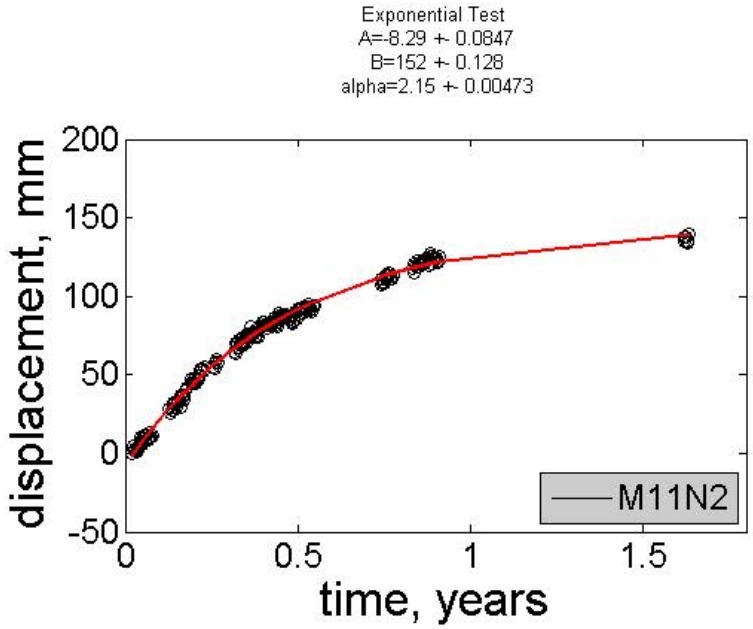

Figure 9: The Exponential relation fit through a MENT synthetic time-series with a normal and random-walk noise

Goodness of fit χ^2 values for this particular synthetic time-series (Exponential, random walk with normal noise) are given in Table 2, and the corresponding relation hierarchy is shown in Figure 10.

Table 2: χ^2 Values, Synthetic MENT, Random Walk and Normal Noise

Relation	χ^2	Relation	χ^2
Linear	1100	Exponential + Linear	34
Logarithmic	320	Modified Omori	34
Logarithmic + Linear	216	Power	61
Exponential	34	Power + Linear	33
Lomnitz	90	Burgers	34
Lomnitz + Linear	32	Modified Omori + Linear	33
GRL	34	GRL + Linear	33

Table 2: Summary of the χ^2 values for the fourteen proposed time-dependencies of postseismic creep. These values were compiled for a synthetic time-series with normal and random noise.

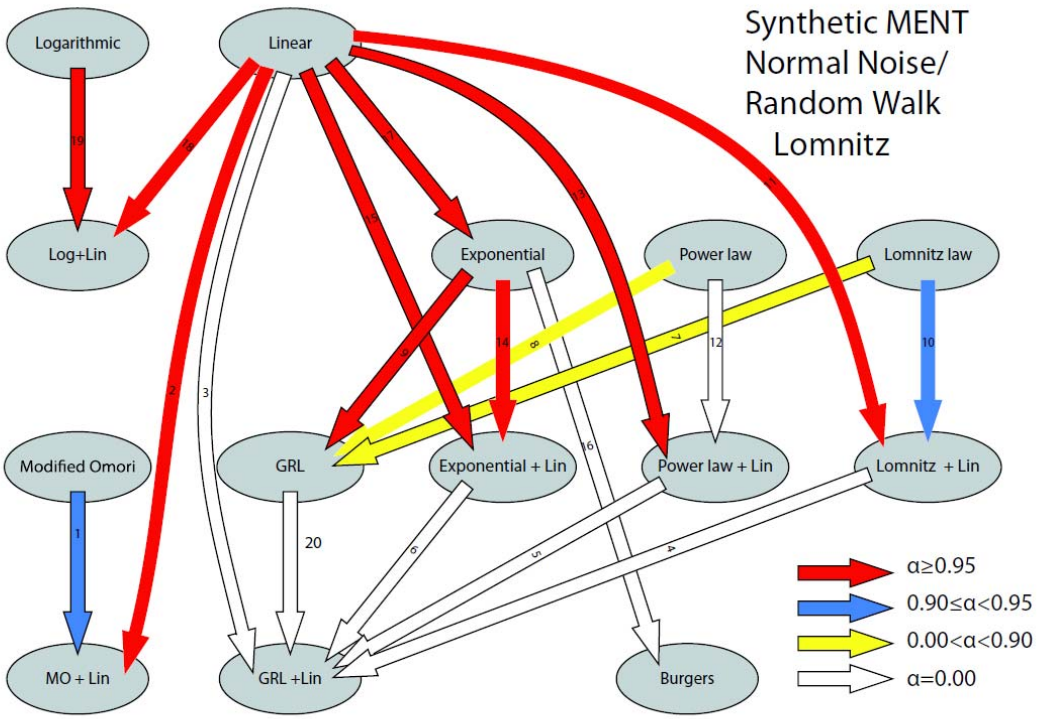

Figure 10: Hierarchy for synthetic MENT time-series. Another hierarchy for a time-series with total displacement amplitude similar to the MENT time-series. Here the noise level is that of a normal and/or random walk present in the time-series. Note the large shift in the α values (and hence, the colors of the arrows) with even just a moderate amount of noise added to the time-series.

Notice the change in the hierarchy with the added random and normal noise. Also notice that the χ^2 values in Table 2 are generally much larger than in Table 1. No relation has a smallest value of χ^2 in Table 2. Also, from Fig. 10, it is clear that the desired Exponential relation clearly is not the best relation of the fourteen considered here. The GRL seems to provide a significantly better fit than the Exponential relation. Hence, any actual real-life time-series, such as those following the Parkfield and Denali events are too noisy to make any valid conclusions here. This example shows that even with just normal noise and some random walk injected into the time-series, the inference of which function best represents the time-series based on the partial F analysis fluctuates wildly. The Partial F Test is too sensitive the level of noise in the actual time-series to be useful. Hence, it is not possible to use the statistical analysis developed here to compare the relations and determining which of them best fit a particular time-series.

Appendix C reports tables of parameter values, their errors, and their χ^2 values. Appendix C also gives tables of parameter values and their corresponding hierarchies for synthetic tests created out of both the Lomnitz and Exponential relations. Hence, there are sixteen tables (and hierarchies) in Appendix C, four tables (for the four noise realizations) with a MENT amplitude created from the Exponential relation, four more tables for MENT created from the Lomnitz relation, four for a FAIR amplitude created from the Lomnitz relation, and four tables with a FAIR amplitude created from Lomnitz.

VIII. Results based on the GRL with a Linear Trend

As the partial F test has proven to be unable to determine which the fourteen possible displacement laws best represents a given GPS time-series, I pursued an alternative approach to search for a systematic difference between the Denali and Parkfield records: I compared fits made to each time-series using *only* the GRL relation with an added linear trend (GRL+L) (equation 1). This relation was chosen for its versatility in that it can account for a wide range in rheologies by adjusting its stress exponent ξ (Section IV). By adding a linear trend, we can study long-term remote tectonic contributions to the postseismic signal. Rheological inferences can be made by comparing the ξ values for multiple time-series for the Parkfield and Denali events.

In this project we defined a signal-to-noise ratio (SNR) is defined as the ratio of the total displacement of a particular record (over the ~1.6 year time span following each event) to the mean noise in the record. The noise was fairly consistent going across the time-series for both records, while the amplitude of particular records amplitude varied greatly. Two of Parkfield's records, USLO and LCOV, had very low SNRs, indicating small amplitudes of displacement when compared to the other Parkfield time-series. This makes sense, as USLO and LCOV were much further than the main Parkfield fault than the other stations analyzed. The time-series for the Parkfield event are shown on the map in Figure 11, and displacement data are plotted for the LCOV and HOGS time-series in Figure 12.

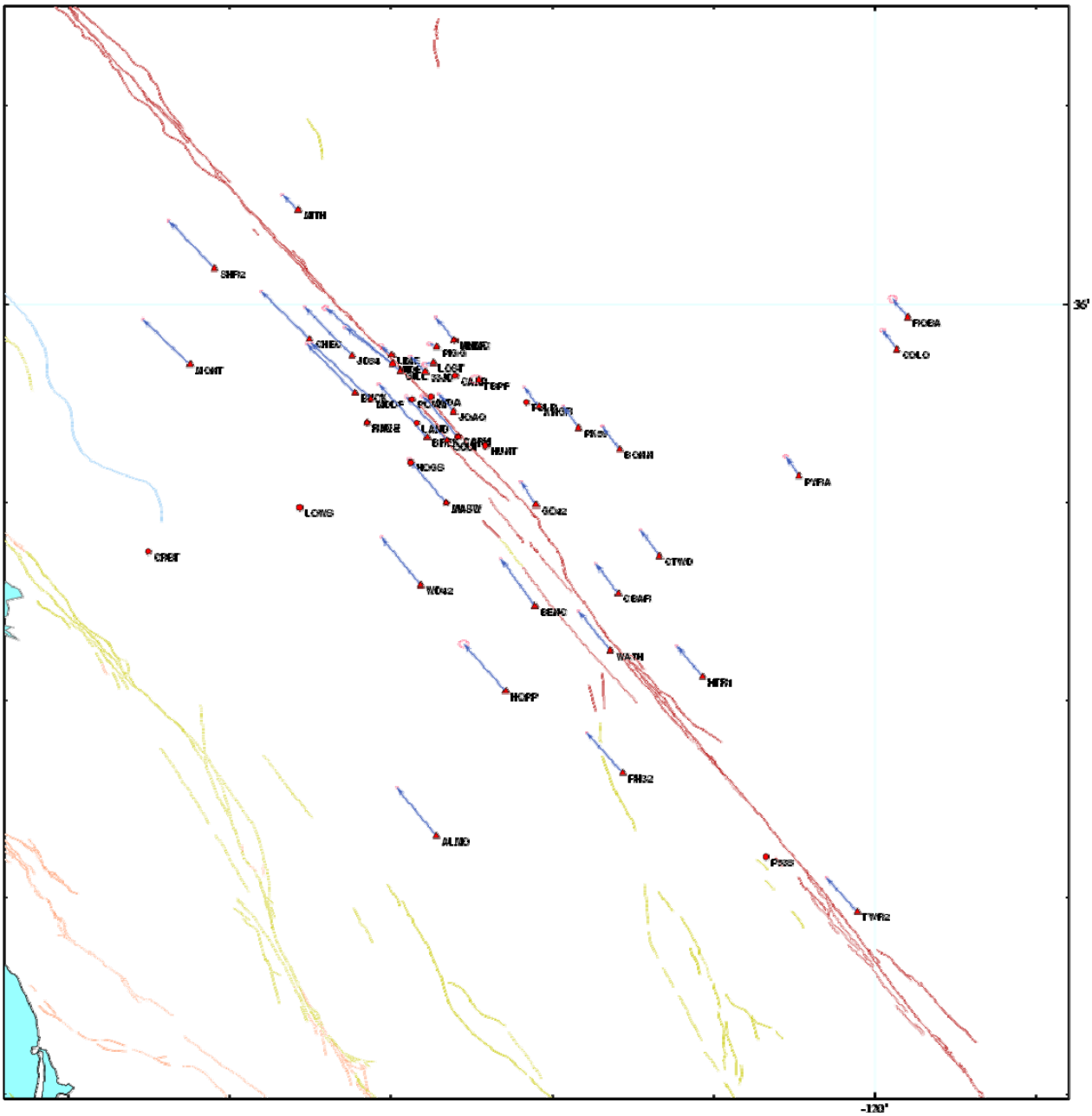

Figure 11: GPS velocities following the Parkfield event. These velocities range a timespan several years following the 28 September 2004 event. Running roughly from the top-left corner down to the bottom right is the main Parkfield fault. The time-series for the USLO (much further to the southeast) and LCOV (much further to the northwest) (both of which are not shown) GPS stations, both with low SNRs, are far away from the main Parkfield fault and are not shown.

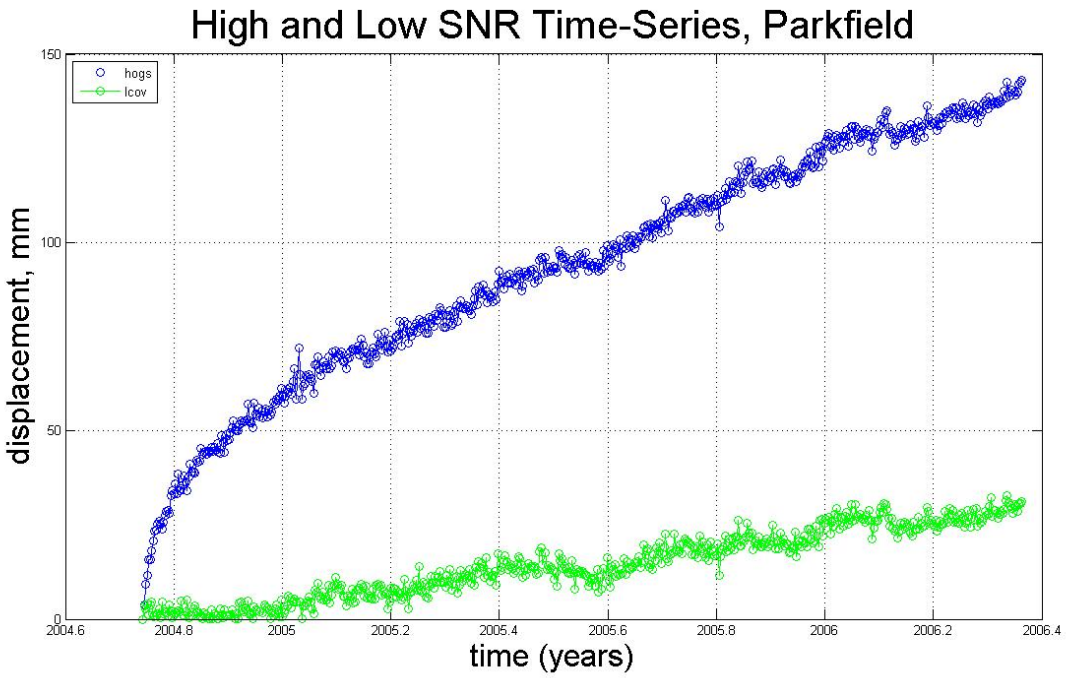

Figure 12: Displacements following the Parkfield earthquake for the LCOV (green) and HOGS (blue) time-series. HOGS was very close to the fault, while the LCOV station was far to the northwest. Note that the HOGS time-series has a much higher amplitude of displacement, and hence a much higher SNR.

Outputted parameter values and their respective errors, along with χ^2 values, were constrained by the Levenberg-Marquardt (LM) inversion routine. SNR values for each GPS record were calculated by taking the total displacement of the record (in mm), and dividing through by the mean uncertainty in that particular time-series. The mean uncertainty was a propagated error that took into account the individual error reported by USGS in both the eastward and westward displacements of each time-series. Hence, if the displacement *D* is a function of both the individual eastward and westward components of the record, then the mean uncertainty is defined as $< \sigma_D >$, the average of the error in the displacements. This error is generally defined as Equation 10,

$$\sigma_D = \sqrt{\left(\frac{\partial D}{\partial D_E}\sigma_E\right)^2 + \left(\frac{\partial D}{\partial D_N}\sigma_N\right)^2} \quad , \tag{10}$$

where D_E and D_N are the displacements in the eastward and northward components and σ_E and σ_N are their errors, respectively. Table 3 summarizes the parameter values, SNR, χ^2 and ξ values, and ratios of v_L / V_0 for Parkfield. Note that most of the ratios of v_L / V_0 are very close to zero, indicating only a small linear trend seen in the Parkfield records analyzed here. Note the huge errors in the parameters and v_L / V_0 for USLO and LCOV. Ultimately the fits to these stations yielded parameter values that lacked physical meaning.

Table 3: A table summarizing parameter values, χ^2, v_L / V_0, and SNRs for the Parkfield time-series. These were compiled using the GRL+L relation (1). Notice how the values for LCOV and USLO seem to deviate from those of the other Parkfield time-series. Such values probably lack physical meaning here, which is reflective of the huge error associated. The error in v_L / V_0 was computed by using error propagation with the individual uncertainties in v_L and V_0.

GPS Station	D_0 (mm)	V_0 (mm/yr)	τ (years)	ξ	v_L (mm/yr)	χ^2	v_L / V_0	NR
HOGS	-3.1±1.5	3.0E3±5.9E2	0.0±0.0	0.03±0.02	46±0.62	7.0	0.015±0.0	60
MASW	0.14±1.2	1.9E3±2.9E2	0.01±0.0	0.12±0.03	45±0.67	.5	0.02±0.0	370
PKDB	-16±9E3	1.0E6±2.5E11	0.0±0.0	-0.32±0.04	39±1.3	.2	0.0±0.10	50
RNCH	-11±6.0	1.7E4±2.2E4	0.0±0.0	-0.17±0.02	41±0.66	2	0.0±0.0	80
LOWS	-2.2±1.3	1.2E3±510	0.0±0.0	-0.03±0.06	47±0.68	.2	0.04±0.02	40
POMM	-8.4±0.80	9.4E3±810	0.0±0.0	-0.02±0.01	44±0.32	0	0.0±0.0	10
CARH	-4.4±0.43	8.0E2±34	0.039±0.0	0.15±0.03	41±1.0	.5	0.05±0.00	90
LAND	-5.5±1.8	5.8E3±1.1E3	0.0±0.0	0.01±0.02	46±0.57	.5	0.01±0.0	10
USLO	-0.5±0.26	4.6E2±1.1E5	15±3.6E3	-120±3E4	-395±1E5	.6	-0.9±330	7
LCOV	-0.2±0.72	34±5.2E3	-0.025±24	50±5.8E3	-21±4.7E3	.8	-0.6±170	4

In general, the Denali records had much smaller values of the SNR due to smaller amplitudes of displacement than the Parkfield records, and hence, generally smaller SNR values. The Denali records also contained fewer displacement data points on average. Some of Denali's records contained as few as forty-six displacement points. Figure 13 shows the time-series of Denali, in relation to the main Denali fault (solid red line) in south-central AK. Note the large distance the FAIR station is from the main fault.

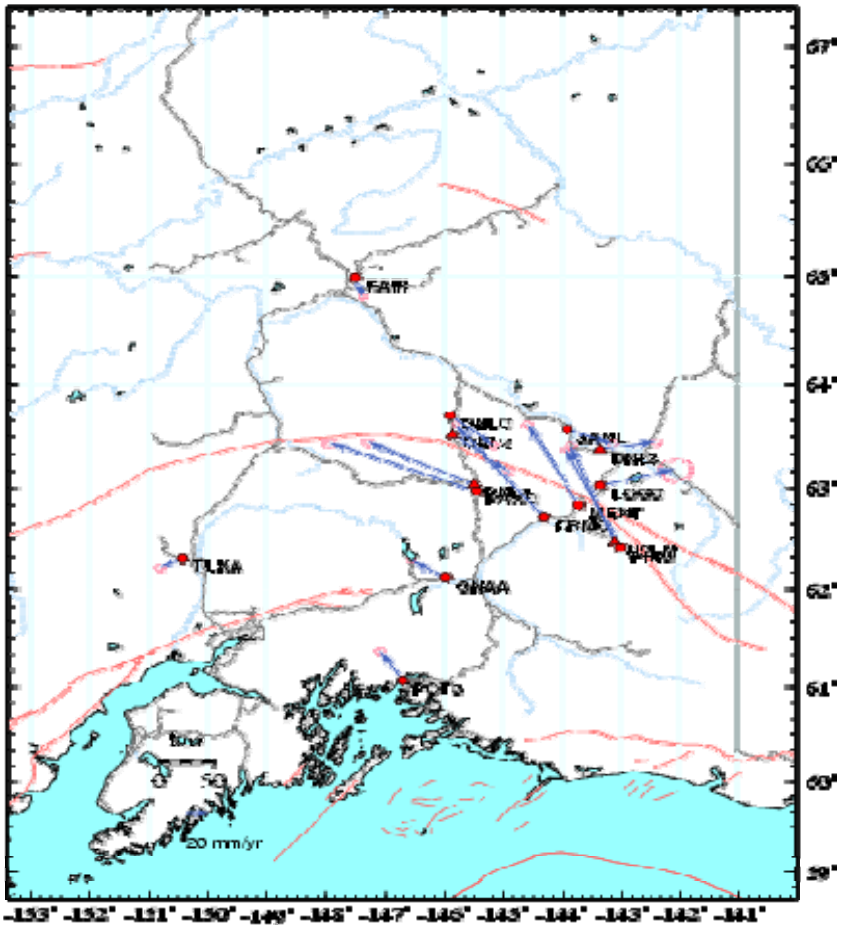

Figure 13: Locations of the GPS time-series relative to the main Denali fault (solid red line), south-central Alaska (USGS). Blue arrows indicate the continuous velocities of the stations' movement in the postseismic interval. Notice that stations located far away from the main fault (POT3, FAIR, TLKA) have random displacement magnitudes and directions that do *not* follow a similar trend to those very close to the main fault, like MENT.

Like Parkfield, some Denali stations had much smaller SNR values than other Denali stations. Figure 14 shows displacements of the MENT time-series plotted against the FAIR times-series. Note that MENT, a station much closer to the main Denali fault, had a much larger total amplitude of displacement than FAIR, which is located much further to the north (Figure 13). Hence, FAIR had a much smaller SNR value than that of MENT.

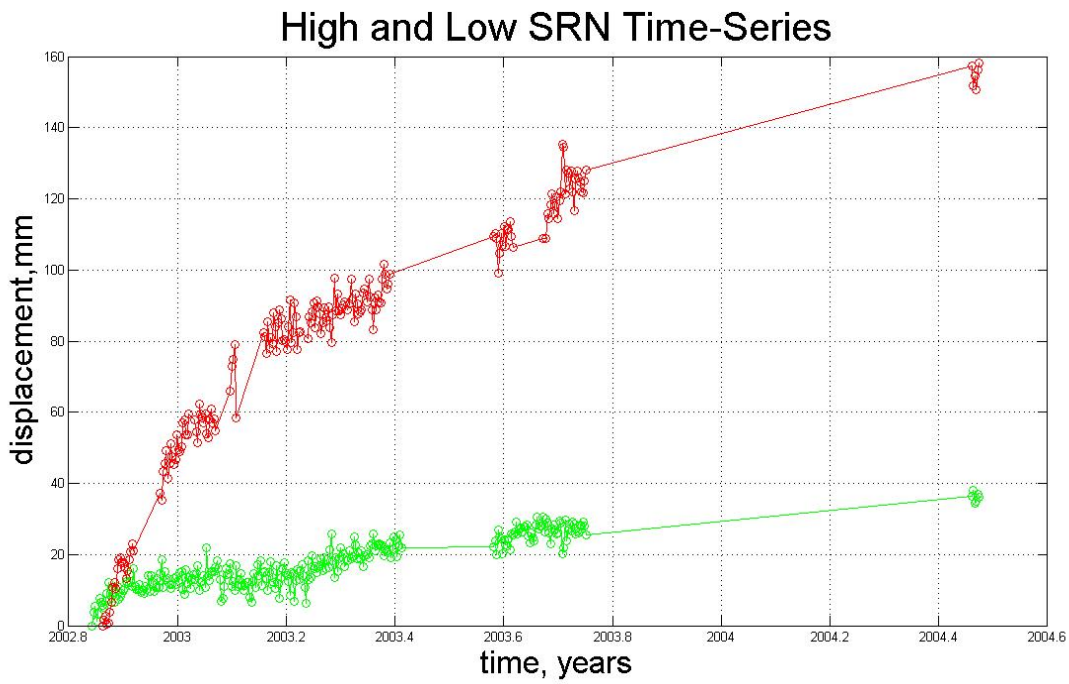

Figure 14: High and low SNR time-series for the Denali event. Red is the for MENT, green for FAIR. Note that MENT has a much greater amplitude of displacement than the FAIR station. The FAIR time-series was much further north away from the main Denali fault (Figure 13), whereas the MENT time-series was just below the fault.

Table 4 summarizes the parameter values, SNR, χ^2 and ξ values, and ratios of v_L / V_0 for Denali. Note that Denali generally has much smaller SNR values than Parkfield, but generally higher values of v_L / V_0.

Table 4: A table summarizing parameter values, χ^2, v_L / V_0, and SNRs for the Denali time-series. These were compiled using the GRL+L relation (1). Generally, the Denali time-series had much lower SNRs here. This is reflected in the huge errors on some of the parameter values, which may even be larger than the parameters themselves. Such values probably lack physical meaning here, which is reflective of the huge error associated. The error in v_L / V_0 was computed by using error propagation with the individual uncertainties in v_L and V_0.

GPS Station	D_0 (mm)	V_0 (mm/yr)	τ (years)	ξ	v_L (mm/yr)	χ^2	v_L / V_0	NR
MENT	-16±1.7	6.9E2±64	0.10±0.01	0.61±0.090	43±3.25	5.3	0.06±0.01	7
USLM	-7.2±2.4	7.5E2±1.0E2	0.11±0.040	0.93±0.25	54±3.6	4.0	0.07±0.01	1
FAIR	6.4±7.8	3.9E2±5.8E4	0.0±12	-53±3.2E3	-310±2E4	0.89	0.07±0.01	.4
GNAA	-0.23±0.31	140±5.0	0.18±0.01	1.2±0.01	15.2±0.71	0.30	0.11±0.01	.6
POT3	-2.7±0.80	110±50	0.10±0.10	0.49±1.2	7.0±14	8.3	0.06±0.13	2
TLKA	8.6±2.6	64±440	0.06±15	1.7±3.3E2	-17±4.9E2	5.3	-0.27±7.88	.9
FRIG	-12±2.7	5.9E2±1.2E2	0.08±0.02	0.70±0.20	72±7.0	2.9	0.12±0.03	7
PAXC	-0.32±0.21	5.8E2±1.3E2	0.68±0.10	0.84±0.90	-260±130	94	-0.45±0.24	7
DNLC	5.4±1.4	2.5E2±45	0.08±0.02	0.36±0.15	4.47±2.62	110	0.02±0.01	2
DRMC	0.86±1.0	360±91	0.59±0.76	0.53±0.79	1.4±79	570	0.0±0.22	2

Hence a greater linear trend is seen in the Denali time-series than for the Parkfield time-series. This is more clearly seen in Figure 15, which shows values of v_L / V_0 for Parkfield and Denali against their SNR values. A greater linear trend contribution is clearly seen in the Denali times-series.

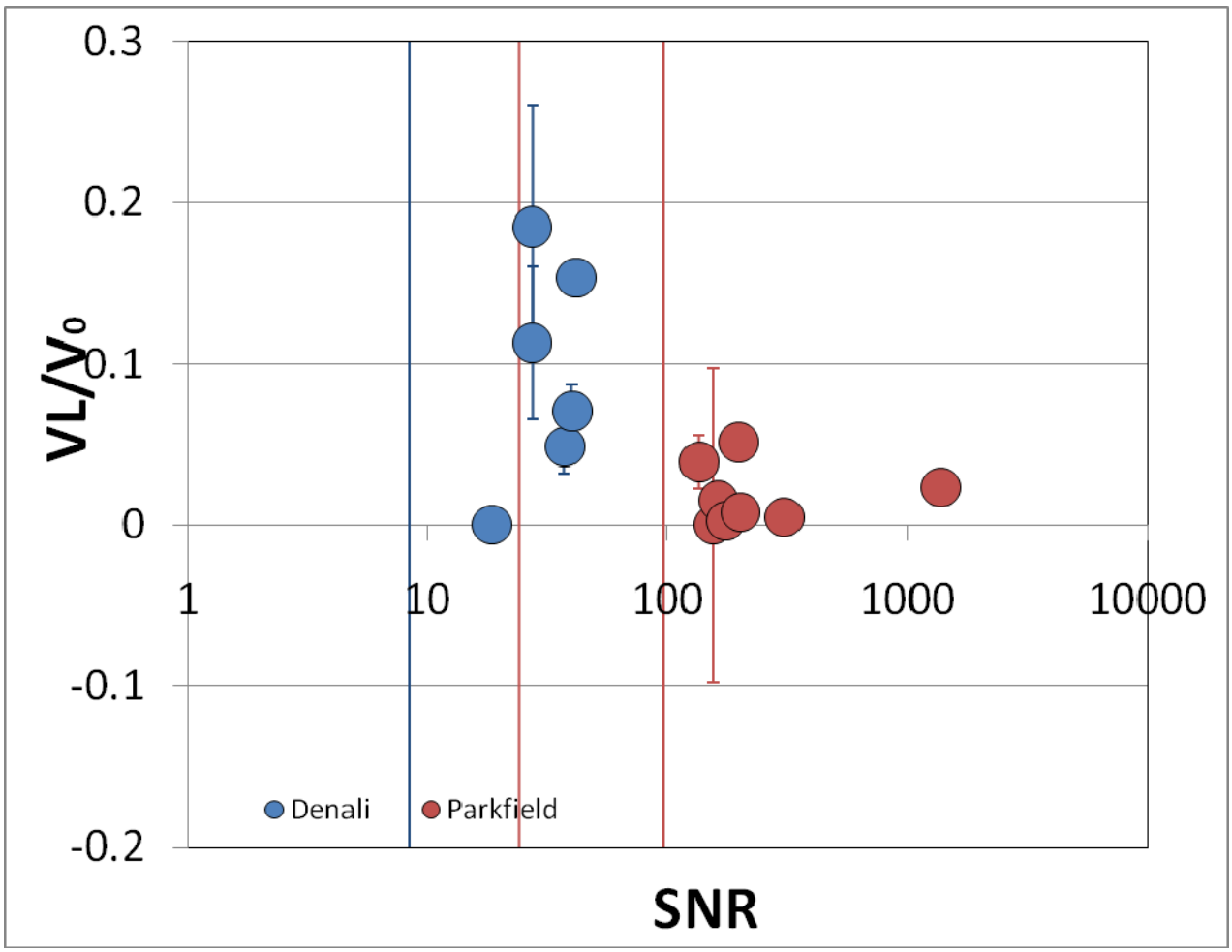

Figure 15: v_L / V_0 values for the Parkfield and Denali events plotted against SNRs. Each dot represents a particular time-series seen in Figures 13 (Denali) and 11 (Parkfield), red for Parkfield, blue for Denali. Note that a greater linear trend is present in the Denali time-series If the error bar is not seen on a particular point, then the error is small enough to be within the point itself.

Figure 16 shows ξ values plotted against SNRs for both the Denali and Parkfield events. Records with low SNR are generally unreliable, but it is clear that for SNR above a particular critical value, records for each earthquake give consistent results: ξ is between 0.5 and 1 for Denali data whereas ξ is between 0 and 0.4 for the Parkfield data.

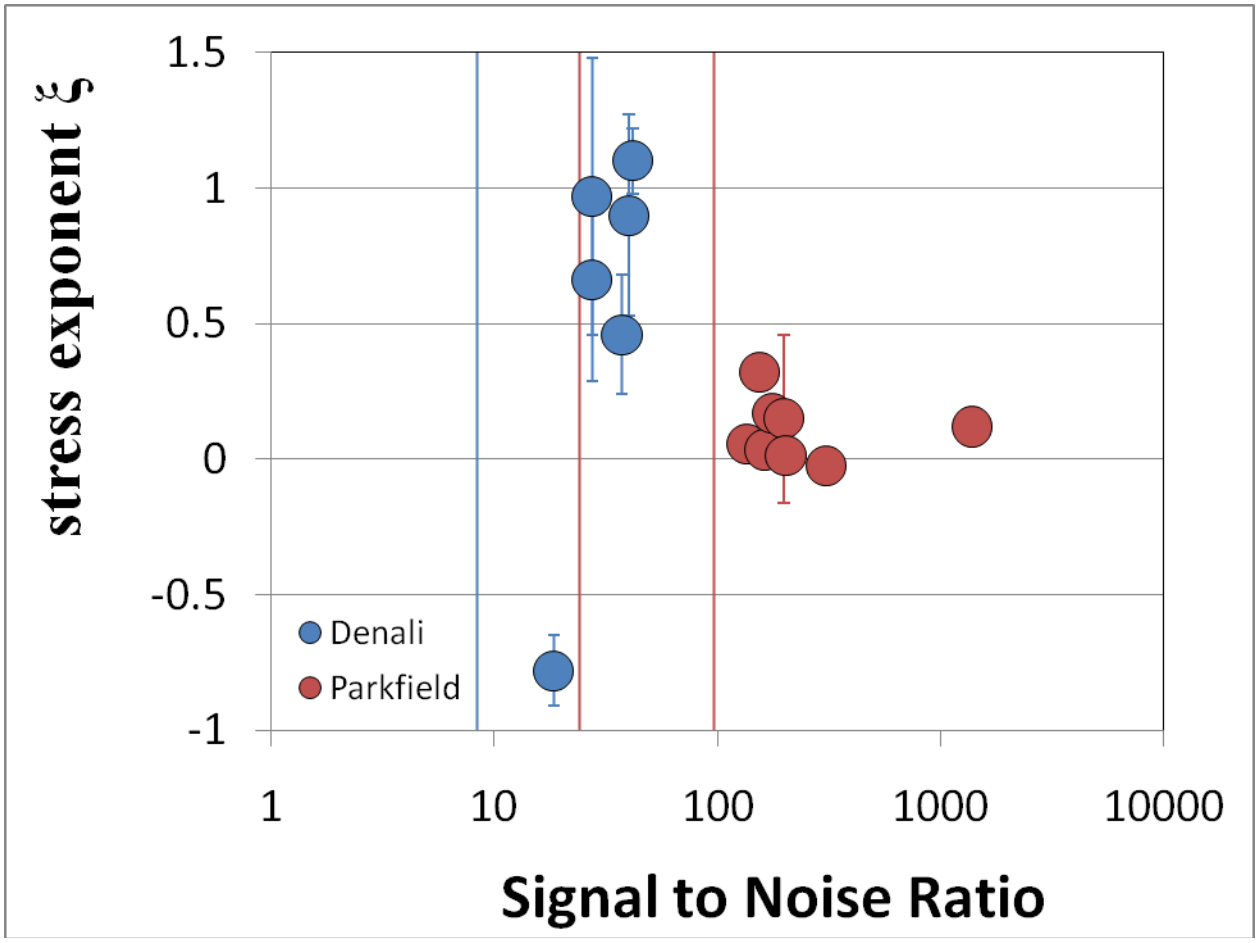

Figure 16: SNR values against 1/*n*. Blue dots are for the Denali event, while red dots are for the Parkfield event. Notice that the Denali cluster indicates that on average, Denali's time-series had much higher mean uncertainties and hence *lower* SNRs. Notice that the Denali points tend to have much higher uncertainties, as given by the vertical error bars. If error bars are not shown on a dot, then the uncertainty is small enough in that it is within the dot itself, as was the case for most of the Parkfield data present here. Evidently the Denali time-series contained much more noise in the dataset, rendering fits more difficult to its time-series. Errors in the values of ξ are given by the LM algorithm (see Appendix B), and values are present in the Appendix D data tables.

Despite lower SNRs, the most important thing to note from Figure 16 are the ξ for the Denali event. In fact, most of the Parkfield ξ values seem to cluster close to zero, while those of Denali seem to cluster closer to a value closer to one. In fact, the average value of ξ for the five Denali time-series clustered close together (blue points in Fig. 16, the PAXC, FRIG, MENT, USLM, DRMC stations) was 0.81, with a standard deviation 0.25. The average ξ value for eight of the Parkfield stations was 0.10, with a standard deviation of 0.11. In this calculation, the LCOV and USLO time-series were not considered, as their extreme fit parameters lacked physical meaning (see the corresponding values in Table 3).

Recall that the GRL relation becomes the Exponential (Newtonian creep in a ductile shear zone, viscous flow) and Lomnitz (rate-dependent friction, afterslip) Laws when we let the stress parameter ξ approach one, and zero, respectively. Hence, by comparing the ξ values between the Parkfield and Denali events using fits made with the GRL relation with the linear trend, there is evidence here that the a Newtonian creep in a ductile shear zone may be contributing most to the postseismic signal observed in the Denali time-series, while brittle aftershocks in the upper crust may be contributing most to the postseismic signal of the Parkfield event.

IX. Conclusions

The Partial F Test applied to our 14-relation hierarchy was ultimately unsuccessful. This resulted from the Partial F Test being far too sensitive to even slight amounts of noise in the data. This was shown as an example with a synthetic time-series (similar amplitude to MENT from Denali), whereas noise was added and very different flow-charts shown. Hence, this particular test was not effective in allowing us to compare *all* 14 displacement functions between both the Parkfield and Denali events, as originally desired. Despite this setback, however, the rheology behind the signals of postseismic relaxation may still be analyzed with the GRL+L relation alone. This relation was able to encompass a range of rheologic behaviors by adjusting a stress parameter ξ. Despite the much higher noise levels in the Denali time-series, which limited our study to only a few its time-series, comparisons were drawn with Parkfield. It was shown that the analyzed Denali ξ values were within a standard deviation of a value of one, indicating a Newtonian creep in a ductile shear zone rheology being more responsible for Denali's signal than brittle mechanisms. The Parkfield time-series, meanwhile, were with a GRL+L with observations fitting a trend showing ξ within a standard deviation of zero. This indicates that brittle mechanisms were most responsible for the signals observed in the vicinity of Parkfield in the postseismic interval. This was consistent with my original hypothesis, whereas the huge energy release of the Denali event was enough to active ductile deformation deep in the crust and/or upper mantle, while the smaller magnitude of the Parkfield active postseismic deformation confined to the upper ~15 km of the crust.

X. Future Work

In this particular area, there is much work to be done. This project was the first of its kind in that it attempted to unify theory as to what particular rheologic mechanisms are most responsible for postseismic signals following the Parkfield and Denali earthquakes. It attempted to test a large number of time-dependencies derived from multiple authors and make reasonable correlations. Perhaps a more refined statistical test less sensitive to noise in GPS time-series would be more effective. If this were to succeed, there would be profound implications to unifying the theory behind understanding earthquake cycle.

XI. Acknowledgements

This project would not have been possible without the guidance, support and patience of Dr. Laurent G.J. Montési, Assistant Professor at the University of Maryland, College Park. He was of great assistance in programming the LM inversion routines to act on the time-series, just as well as proposing the original project and offering it to myself as a senior thesis; I have learned much during this experience about the scientific method.

Appendix A: A Summary of the Fourteen Displacement Functions

Here we provide a table summarizing the fourteen time-dependencies of postseismic creep that were considered in this project. Table A1 is organized such that the number of parameters increasing from two to five parameters going down the rows. A reference is also provided of where the particular law was applied in previous research. Then, on the right, a brief description may be given describing the rheology mechanism behind the postseismic creep. Below Table A1 are links to the USGS from where the raw GPS time-series were obtained.

Table A1

Dependence	Equation	Reference	Rheology
Linear	$D_s(t) = a + bt$		Remote plate motion, postseismic creep from other, earlier earthquakes
Logarithmic	$D_s(t) = a + b\log t$	Savage *et al.*, 2005.	Transient creep, rapid initial displacements
Logarithmic + Linear	$D_s(t) = a + b\log t + v_L t$		
Exponential	$D_s(t) = a + b\exp(-\alpha t)$	Savage *et al.*, 2005	Newtonian creep in a ductile shear zone. Equivalent to GRL $\xi \to 1$
Lomnitz	$D(s) = a + b\log(1+\alpha t)$	Marone *et al.*, 2001; Savage *et al.*, 2005; Savage and Langbein, 2008	Rate-dependent friction Equivalent to GRL $\xi \to 0$
Power	$D_s(t) = D_0 + 3V_0\tau\left(1-\left(1+\frac{2t}{3\tau}\right)^{3/2}\right)$		Dislocation creep in a ductile shear zone; special case of GRL ξ=1/3
Exponential + Linear	$D_s(t) = a + b\exp(-\alpha t) + v_L t$		
Lomnitz + Linear	$D(s) = a + b\log(1+\alpha t) + v_L t$		
Power Law + Linear	$D_s(t) = D_0 + 3V_0\tau\left(1-\left(1+\frac{2t}{3\tau}\right)^{3/2}\right) + v_L t$		
Modified Omori (MO)	$D_s(t) = A + B[1-(1+\alpha t)]^{1-p}$	Savage, 2007; Savage and Yu, 2007	Based on a similarity with aftershock sequences; similar to GRL
General Relaxation Law	$D_s(t) = D_0 + \frac{V_0\tau}{\xi}\left(1-\left(1+(1-\xi)\frac{t}{\tau}\right)^{\frac{1}{1-1/\xi}}\right)$	Montési, 2004	Power-law creep in a ductile shear zone.
Modified Omori + Linear	$D_s(t) = A + B[1-(1+\alpha t)]^{1-p} + v_L t$		

General Relaxation Law + Linear	$D_s(t) = D_0 + \frac{V_0\tau}{\xi}\left(1 - \left(1 + (1-\xi)\frac{t}{\tau}\right)^{\frac{1}{1-1/\xi}}\right) + v_L t$		
Burgers	$D_s(t) = a + b_1 \exp(-\alpha_1 t) + b_2 \exp(-\alpha_2 t)$	Hetland and Hager, 2006; Burgmann and Dresen, 2008	Burgers body rheology, Maxwell fluid and Kelvin body assembled in series.

A link to the USGS Denali time-series:
http://earthquake.usgs.gov/monitoring/gps/Denali/
A link to the USGS Parkfield time-series:
http://earthquake.usgs.gov/monitoring/gps/Parkfield/

Appendix B: The Levenberg-Inversion Routine and the GPS Time-Series

Here, we give a more detailed description on how the Levenberg-Marquardt (LM) inversion routine acted on a particular downloaded USGS time-series. We used a LM inversion routine to solve the least-squares problem and provide the best fit χ^2 to the time-series for each displacement function. Our GPS datasets consisted of, say, U pairs (t_i, D_i), for i = 1, 2, … U, where D_i (displacement) is a function of time t_i. The number of data points varied anywhere from ~50 to ~600 data points for the *same* time interval (~1.6 years) following both the Parkfield and Denali events. Each downloaded data set contained eastward and northward components for D_i, both of these components yielding data pairs with t_i as the independent variable.

Each of the fourteen functions had the form $D_S(t_i, \vec{Z})$, with N adjustable parameters stored in a vector $\vec{Z}$. To find the parameter values for a best fit, we considered when the sum of the squared residuals is minimized. The residual in our case is $r_i = D_i - D_S(t_i, \vec{Z})$. We solved this problem of least-squares here by invoking the iterative LM inversion routine (Press *et al.*, 1992), as was applied by Montési (2004) with the GRL relation to postseismic time-series for several events. A derivation of the LM inversion routine and its applicability to our least-squares problem is provided shortly. When the number of adjustable parameters N is constrained by the LM algorithm to minimize the residuals, a measure of the goodness of a fit is given by (11):

$$\chi^2 = \sum_{i=1}^{U}\left[\frac{D_S(t_i) - D_S(t_i, \vec{Z})}{E_i}\right]^2 \qquad (11)$$

In (11), E_i is the formal uncertainty for each data point. This is represented graphically in the plots by a vertical bar in each displacement point. If the inversion routine is to minimize our squared

residuals between the predicted value given by one of the fourteen relations and the actual data point, an initial guess for parameter values in the vector $\vec{Z}$ must be provided. Then, the increment of each parameter in $\vec{Z}$ is set to some value between two end members: a steepest descent and an inverse Hessian method, which both use the first and second partial derivatives of (11) in our parameter space. An example for this method as applied to the Power Law function (3 parameters) follow and its application to the nonlinear least squares problem.

If the LM inversion (Press *et al*., 1992) routine is to minimize the squared residual in (11), an initial guess for the parameter values in $\vec{Z}$ must be provided. Each iterative step makes our parameter vector $\vec{Z}$ become, for some η, which is found by approximating $D_S(t_i, \vec{Z}+\eta)$ as in the linearization (12) (below):

$$D_S(t_i, \vec{Z}+\eta) \approx D_S(t_i, \vec{Z}) + J_i\eta \qquad (12)$$

$$J_i = \frac{\partial D_S(t_i, \vec{Z})}{\partial \vec{Z}}$$

The second expression in (12) is the Jacobian of $D_S(t_i, \vec{Z}+\eta)$. For example, the following are the Jacobian for the 3-parameter Power Relation given by equation (3), which consists of partial derivatives with respect to each of the three parameters stored in the vector $\vec{Z}$, which are given below:

$$\vec{Z} = \begin{bmatrix} Z_1 \\ Z_2 \\ Z_3 \end{bmatrix} = \begin{bmatrix} D_0 \\ V_0 \\ \tau \end{bmatrix}$$

$$\frac{\partial D_S(t_i, \vec{Z})}{\partial D_0} = 1$$

$$\frac{\partial D_S(t_i, \vec{Z})}{\partial V_0} = 3\tau\left(1 - \left(1 + \frac{2t}{3\tau}\right)^{3/2}\right)$$

$$\frac{\partial D_S(t_i, \vec{Z})}{\partial \tau} = 3V_0\left[\left(1 - \left(1 + \frac{2t}{3\tau}\right)^{3/2}\right) - 3\tau\left(1 + \frac{2t}{3\tau}\right)^{1/2}\right]$$

When the sum of squares (11) is minimized, the partial derivative of (12) (with respect to η) is zero. Upon differentiating the squared residuals in (11) using the linearization given by (12), we obtain (13). The right side of the equation gives us a vector notation. Upon taking the derivative of (12) with respect to η and setting the expression to zero, we also obtain (14):

$$S(\vec{Z}+\eta) \approx \sum_{i=1}^{U}(D_i - D_S(t_i,\vec{Z}) - J_i\eta)^2 = \left\| \vec{D}_i - \vec{D}_S(\vec{Z}) - \vec{J}\eta \right\|^2 . \quad (13)$$

$$(\vec{J}^T \vec{J})\eta = \vec{J}^T [\vec{D}_i - \vec{D}_S(\vec{Z})] \quad (14)$$

From (11) we can obtain a set of linear equations that is solved for η. In (14), $\vec{J}$ is a Jacobian matrix containing partial derivatives with respect to each parameter in $\vec{Z}$. Each *i*th row in $\vec{J}$ is $\vec{J}_i$ and $\vec{D}_S$ is a vector within the *i*th $D_S(t_i,\vec{Z}+\eta)$ and data point $\vec{D}_i$. Both Levenberg and Marquardt modified (14) to give the inversion algorithm we perform on the postseismic time-series we use here. An alternate version of (14) offered by Levenberg and Marquardt as given by (15). This gives us the increment η that we seek. The damping factor φ in (15) is slightly adjusted with each iteration.

$$(\vec{J}^T \vec{J} + \varphi diag(\vec{J}^T \vec{J}))\eta = \vec{J}^T [D_i - D_S(\vec{Z})] \quad (15)$$

Appendix C: GRL+L Data Tables, Synthetic Test Tables, and their Hierarchies

Here are tables of parameter values, their errors, and their χ^2 values for the synthetic datasets. Following each table is the corresponding function hierarchy for the fourteen relations considered in this project. There are sixteen tables (and hierarchies), four tables (for the four noise realizations) with a MENT amplitude created from the Exponential relation, four more tables for MENT created from the Lomnitz relation, four for a FAIR amplitude created from the Lomnitz relation, and four tables with a FAIR amplitude created from Lomnitz.

Table C1: Parameter and χ^2 values for the F10N1 synthetic time-series. It was created with similar total displacement amplitude to FAIR of the Denali network and produced from the Lomnitz Relation. Here there is zero noise.

Function	Parameter 1	Parameter 2	Parameter 3	Parameter 4	Parameter 5	χ^2
Linear	11±0.041	29±0.070				69
Logarithmic	36±0.037	9.8±0.023				52
Logarithmic and Linear	25±0.11	6.1±0.043	14±0.13			12
Exponential	2.9±0.075	43±0.14	1.8±0.015			3.6
Lomnitz	0.11±0.12	18±0.13	8.0±0.18			0.078
Lomnitz and Linear	-0.56±0.15	16±0.39	10.0±0.48	1.3±0.39		0.037
GRL	0.19±0.15	140±3.7	0.14±0.0085	0.077±0.027		0.039
Exponential and Linear	0.97±0.10	26±0.25	3.7±0.064	12±0.23		0.36
Modified Omori	0.33±0.14	130±19	5.2±0.45	1.2±0.038		0.099
Power	0.92±0.099	110±1.2	0.22±0.0032			0.42
Power and Linear	0.17±0.13	130±2.3	0.16±0.0053	4.8±0.37		0.032
Burgers	0.11±0.14	13±0.67	7.0±0.41	43±0.46	0.91±0.049	0.024
Modified Omori and Linear	0.14±0.17	110±81	5.7±1.6	1.2±0.21	1.9±0.21	0.028
GRL and Linear	0.24±0.17	130±7.0	0.16±0.017	0.24±0.14	1.9±2.8	0.069

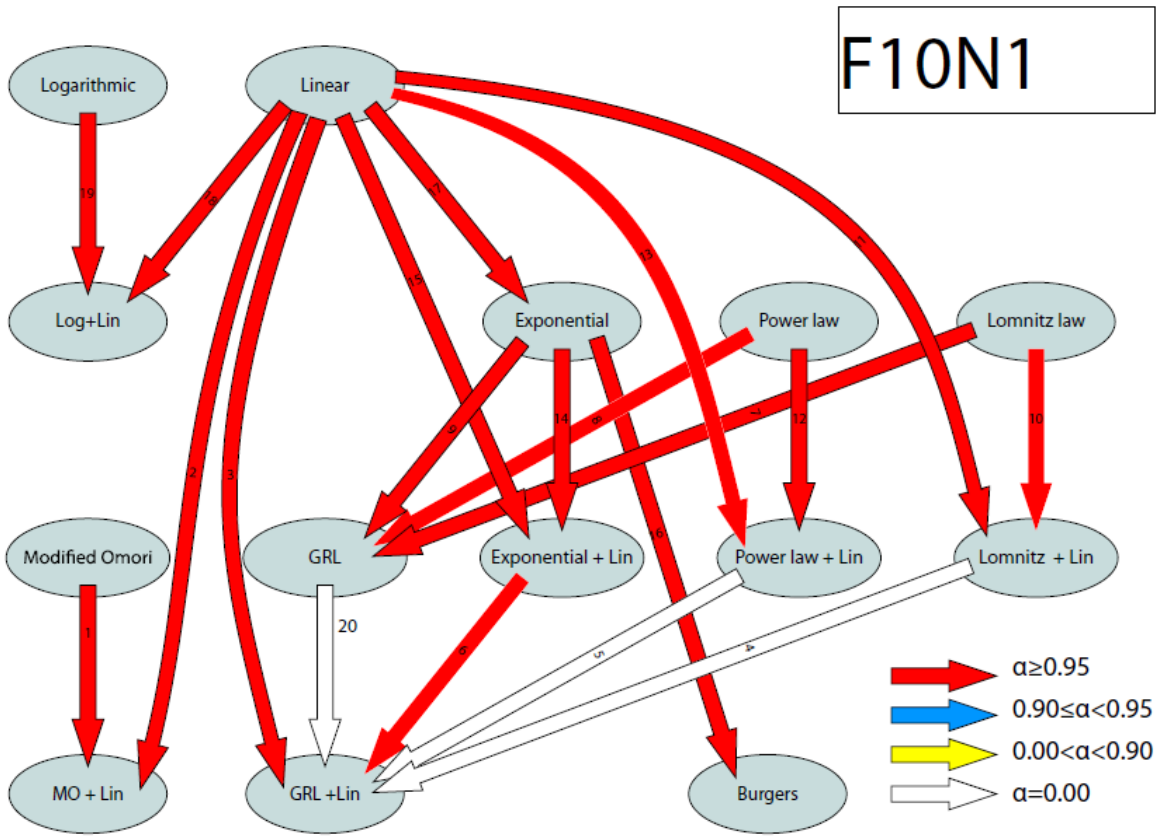

Figure C1: Hierarchy corresponding to Table C1.

Table C2: Parameter and χ^2 values for the F10N2 synthetic time-series. It was created with similar total displacement amplitude to FAIR of the Denali network and produced from the Lomnitz Relation. "N/A" here means that no reasonable fit was able to be obtained. Here there is normal noise and random walk.

Function	Parameter 1	Parameter 2	Parameter 3	Parameter 4	Parameter 5	χ^2
Linear	14±0.069	11±0.12				39
Logarithmic	25±0.062	5.6±0.039				18
Logarithmic and Linear	34±0.20	8.8±0.077	-11±0.23			17
Exponential	0.14±0.20	24±0.19	6.2±0.10			12
Lomnitz	-9.3±1.6	5.7±0.055	450±140			17
Lomnitz and Linear	0.34±0.24	26±0.98	6.9±0.43	-30±0.83		9.9
GRL	N/A	N/A	N/A	N/A		N/A
Exponential and Linear	N/A	N/A	N/A	N/A		N/A
Modified Omori	N/A	N/A	N/A	N/A	N/A	N/A
Power	-4.1±0.42	420±23	0.029±0.0014			16
Power and Linear	N/A	N/A	N/A	N/A		N/A
Burgers	N/A	N/A	N/A	N/A	N/A	N/A
Modified Omori and Linear	N/A	N/A	N/A	N/A	N/A	N/A
GRL and Linear	N/A	N/A	N/A	N/A	N/A	N/A

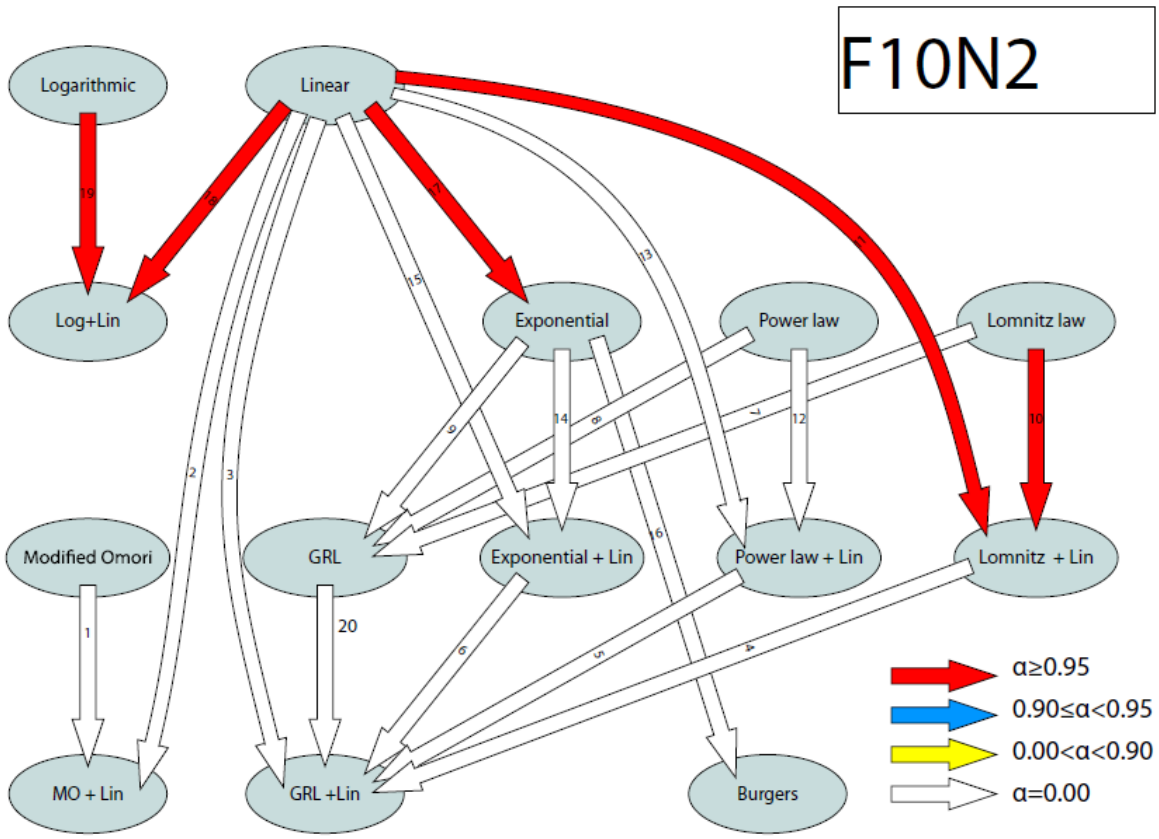

Figure C2: Hierarchy corresponding to Table C2.

Table C3: Parameter and χ^2 values for the F10N3 synthetic time-series. It was created with similar total displacement amplitude to FAIR of the Denali network and produced from the Lomnitz Relation. "N/A" here means that no reasonable fit was able to be obtained. Here there is noise from random-walk only.

Function	Parameter 1	Parameter 2	Parameter 3	Parameter 4	Parameter 5	χ^2
Linear	6.1±0.041	25±0.070				120
Logarithmic	27±0.037	8.0±0.023				170
Logarithmic and Linear	13±0.11	3.0±0.043	18±0.13			110
Exponential	1.9±0.067	44±0.29	1.1±0.014			95
Lomnitz	1.2±0.085	24±0.31	2.6±0.065			95
Lomnitz and Linear	1.6±0.093	51±5.3	1.3±0.12	-12±1.9		95
GRL	1.6±0.092	52±0.91	0.70±0.042	0.67±0.07		95
Exponential and Linear	1.6±0.086	29±1.6	1.6±0.081	6.5±0.82		95
Modified Omori	1.6±0.092	55±3.5	0.46±0.13	3.1±0.67		95
Power	1.4±0.078	56±0.59	0.53±0.010			95
Power and Linear	N/A	N/A	N/A	N/A		N/A
Burgers	1.6±0.086	29±0.0	1.6±0.050	-5.1E6±0.0	6.6E-07±0.0	240
Modified Omori and Linear	N/A	N/A	N/A	N/A	N/A	N/A
GRL and Linear	N/A	N/A	N/A	N/A	N/A	N/A

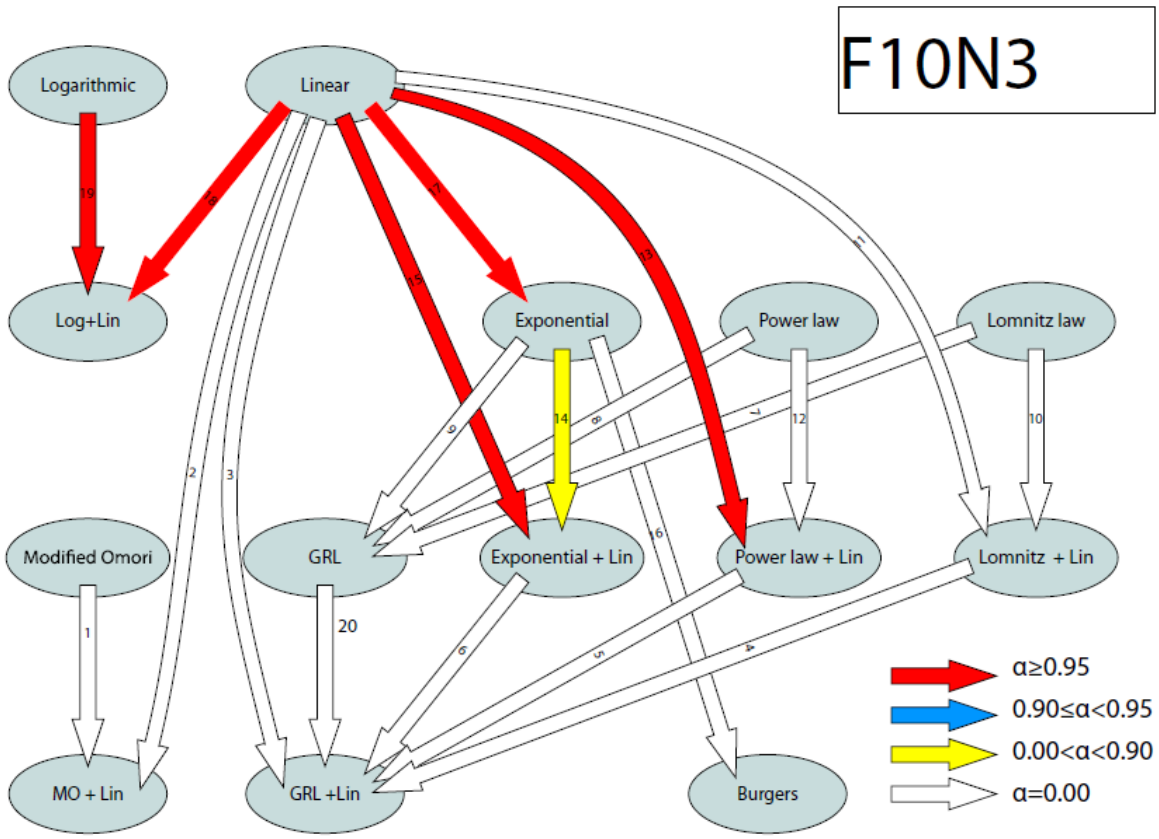

Figure C3: Hierarchy corresponding to Table C3.

Table C4: Parameter and χ^2 values for the F10N4 synthetic time-series. It was created with similar total displacement amplitude to FAIR of the Denali network and produced from the Lomnitz Relation. "N/A" here means that no reasonable fit was able to be obtained. Here there is noise is normal noise only.

Function	Parameter 1	Parameter 2	Parameter 3	Parameter 4	Parameter 5	χ^2
Linear	4.5±0.18	18±0.30				3.4
Logarithmic	19±0.16	5.8±0.096				4.7
Logarithmic and Linear	11±0.47	2.6±0.19	11±0.56			3.1
Exponential	0.50±0.30	28±0.78	1.5±0.093			2.5
Lomnitz	0.36±0.38	15±1.0	3.3±0.50			2.6
Lomnitz and Linear	0.96±0.33	460±730	0.27±0.25	-88±82		2.4
GRL	N/A	N/A	N/A	N/A		N/A
Exponential and Linear	0.92±0.33	120±140	0.53±0.36	-29±30.0		2.4
Modified Omori	0.52±0.29	28±0.85	6.5E-8±0.038	2.2E7±1.1E13		2.5
Power	4.5±0.18	18±0.30	1.9E13±0.30			3.4
Power and Linear	4.5±0.18	11±29	5.9E13±4.8E13	6.9±29		3.4
Burgers	N/A	N/A	N/A	N/A	N/A	N/A
Modified Omori and Linear	N/A	N/A	N/A	N/A	N/A	N/A
GRL and Linear	N/A	N/A	N/A	N/A	N/A	N/A

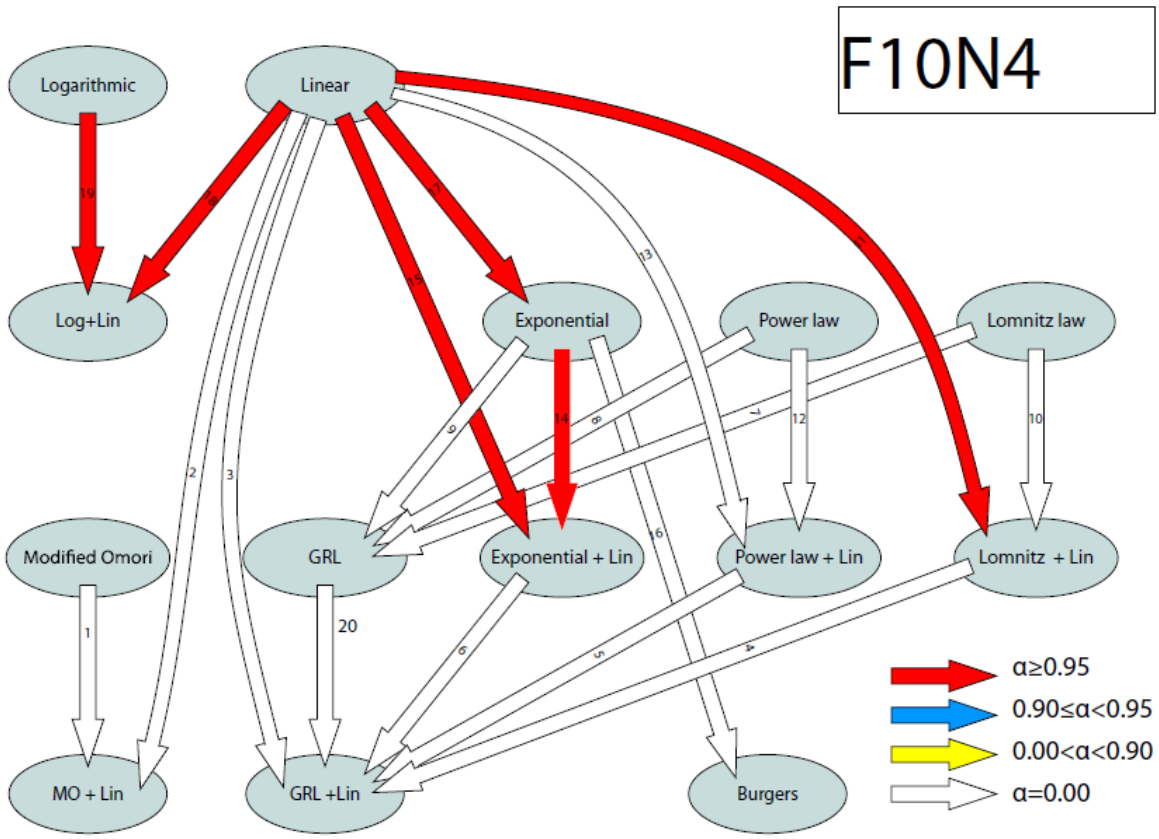

Figure C4: Hierarchy corresponding to Table C4.

Table C5: Parameter and χ^2 values for the F11N1 synthetic time-series. It was created with similar total displacement amplitude to FAIR of the Denali network and produced from the Exponential relation. "N/A" here means that no reasonable fit was able to be obtained. Here there is a zero noise level.

Function	Parameter 1	Parameter 2	Parameter 3	Parameter 4	Parameter 5	χ^2
Linear	9.9±0.041	32±0.070				100
Logarithmic	38±0.037	11±0.023				81
Logarithmic and Linear	26±0.11	7.0±0.043	15.0±0.13			34
Exponential	0.15±0.078	48±0.12	2.0±0.014			0.0061
Lomnitz	-2.5±0.12	20.0±0.13	8.0±0.16			4.3
Lomnitz and Linear	-0.55±0.10	57±2.0	2.3±0.087	-26±1.0		0.063
GRL	0.21±0.092	93±0.91	0.55±0.013	1.1±0.023		0.080
Exponential and Linear	-0.16±0.088	48±0.88	2.0±0.040	0.17±0.53		0.0084
Modified Omori	-0.47±0.099	51±0.55	0.31±0.061	7.5±1.3		0.094
Power	-1.7±0.098	130±1.2	0.22±0.0028			2.0
Power and Linear	-0.39±0.098	120±0.65	0.46±0.015	-17±0.89		0.075
Burgers	-0.16±0.11	48±15	2.0±0.33	16±3.46E4	0.015±33	0.032
Modified Omori and Linear	-0.45±0.13	270±503	1.8±0.87	1.3±0.60	-21±-11	0.043
GRL and Linear	N/A	N/A	N/A	N/A	N/A	N/A

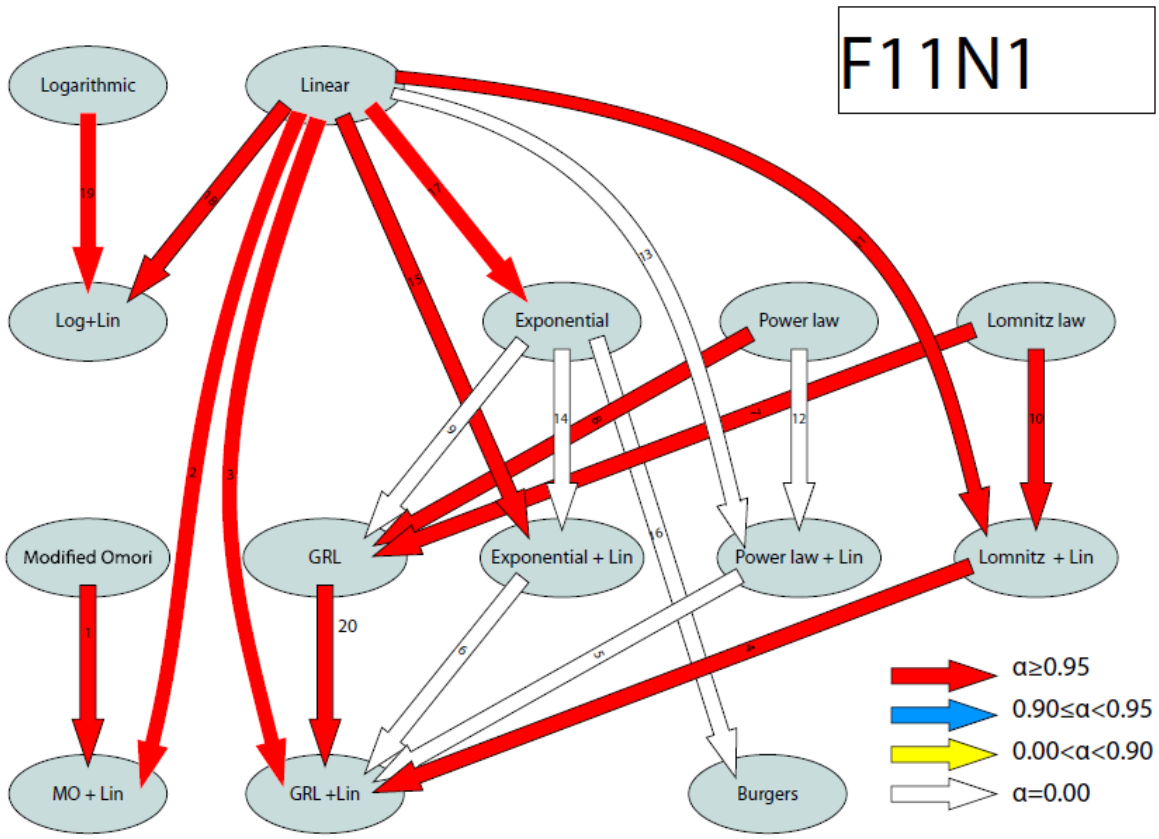

Figure C5: Hierarchy corresponding to Table C5.

Table C6: Parameter and χ^2 values for the F11N2 synthetic time-series. It was created with similar total displacement amplitude to FAIR of the Denali network and produced from the Exponential relation. "N/A" here means that no reasonable fit was able to be obtained. Here there is normal noise and random walk.

Function	Parameter 1	Parameter 2	Parameter 3	Parameter 4	Parameter 5	χ^2
Linear	12±0.086	34±0.15				60
Logarithmic	44±0.077	13±0.050				37
Logarithmic and Linear	42±0.24	13±0.096	1.4±0.28			36
Exponential	-7.1±0.19	53±.18	3.5±0.036			14
Lomnitz	-8.5±0.36	18±0.18	18±0.81			21
Lomnitz and Linear	-5.6±0.22	95±4.2	2.4±0.11	-67±2.2		12
GRL	N/A	N/A	N/A	N/A		N/A
Exponential and Linear	-5.7±0.19	74±1.3	2.4±0.051	17±0.87		12
Modified Omori	N/A	N/A	N/A	N/A		N/A
Power	-8.8±0.27	280±5.8	0.10±0.0024			19
Power and Linear	N/A	N/A	N/A	N/A		N/A
Burgers	N/A	N/A	N/A	N/A	N/A	N/A
Modified Omori and Linear	N/A	N/A	N/A	N/A	N/A	N/A
GRL and Linear	N/A	N/A	N/A	N/A	N/A	N/A

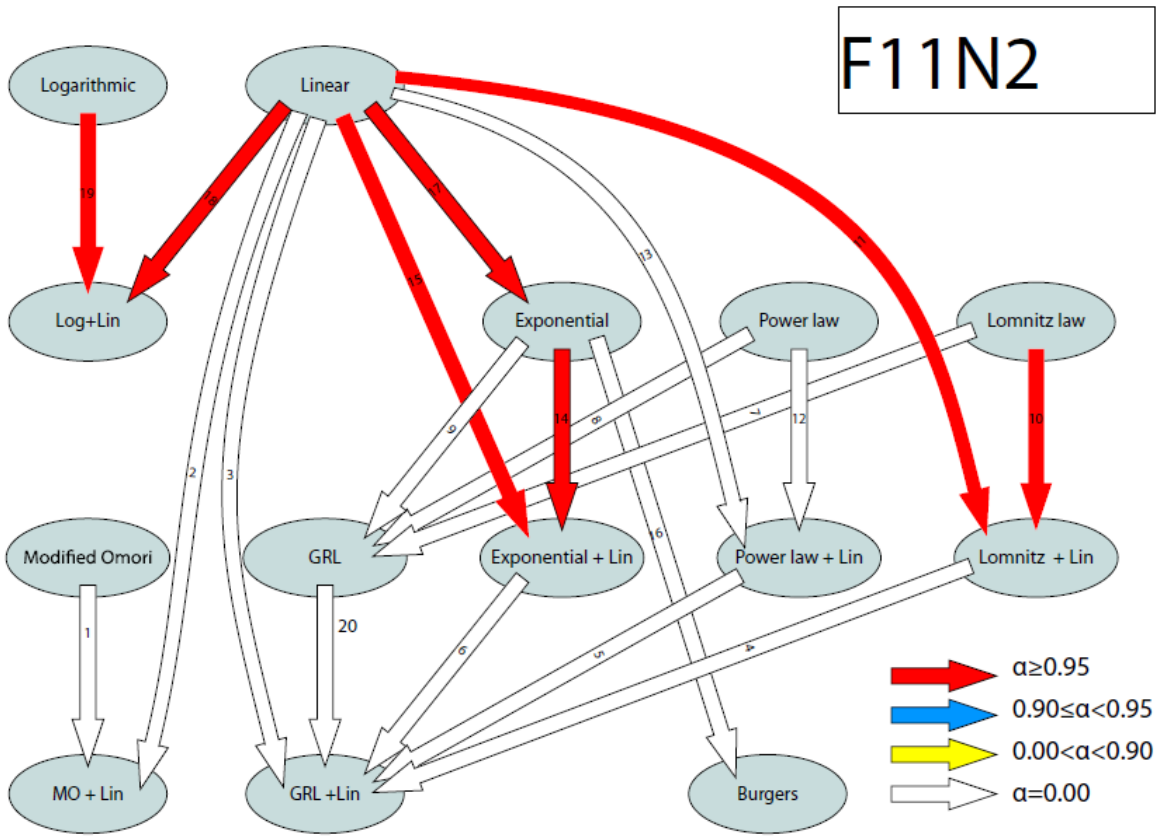

Figure C6: Hierarchy corresponding to Table C6.

Table C7: Parameter and χ^2 values for the F11N3 synthetic time-series. It was created with similar total displacement amplitude to FAIR of the Denali network and produced from the Exponential relation. "N/A" here means that no reasonable fit was able to be obtained. The noise level is random-walk only.

Function	Parameter 1	Parameter 2	Parameter 3	Parameter 4	Parameter 5	χ^2
Linear	9.5±0.041	30±0.070				196
Logarithmic	36±0.037	11±0.023				180
Logarithmic and Linear	25±0.11	6.8±0.043	13±0.13			130
Exponential	-0.81±0.079	45±0.11	2.2±0.015			92
Lomnitz	2.7±0.12	19±0.12	8.6±0.17			99
Lomnitz and Linear	-0.63±0.099	71±2.8	1.9±0.072	-35±1.8		92
GRL	-0.41±0.09	92±0.88	0.55±0.012	1.9±0.021		92
Exponential and Linear	-0.54±0.088	51±0.97	1.9±0.039	-3.5±0.57		92
Modified Omori	-0.81±0.079	45±0.11	5.6E-8±0.0031	3.8E7±2.1E12		92
Power	-2.1±0.10	130±1.3	0.20±0.0026			96
Power and Linear	N/A	N/A	N/A	N/A		N/A
Burgers	N/A	N/A	N/A	N/A	N/A	N/A
Modified Omori and Linear	-0.54±0.12	51±9.8	5.1E-3±0.31	380±2.3E4	-3.6±4.1	92
GRL and Linear	N/A	N/A	N/A	N/A	N/A	N/A

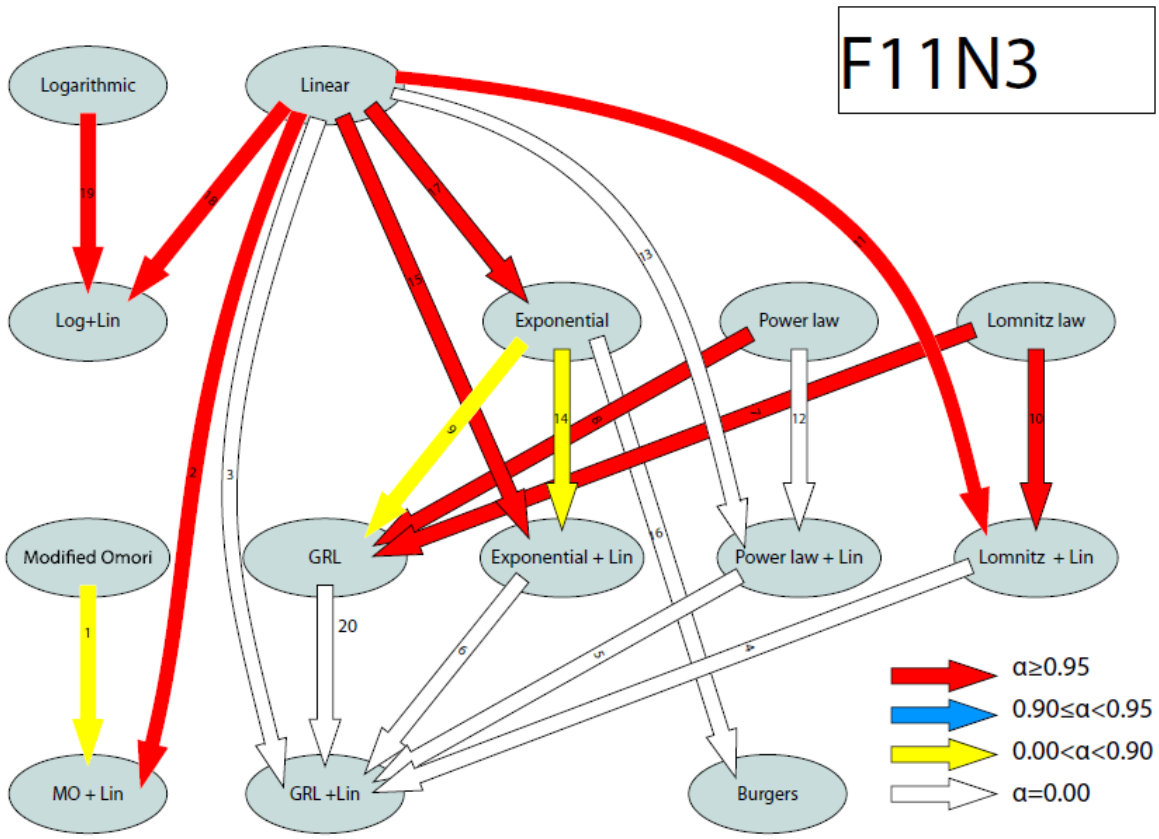

Figure C7: Hierarchy corresponding to Table C7.

Table C8: Parameter and χ^2 values for the F11N4 synthetic time-series. It was created with similar total displacement amplitude to FAIR of the Denali network and produced from the Exponential relation. "N/A" here means that no reasonable fit was able to be obtained. The noise level is normal noise only.

Function	Parameter 1	Parameter 2	Parameter 3	Parameter 4	Parameter 5	χ^2
Linear	-2.0±0.22	-49±0.36				10
Logarithmic	38±0.19	14±0.12				28
Logarithmic and Linear	-4.7±0.60	-1.2±0.24	53±0.70			10
Exponential	20±0.13	-8.6E-9±3.7E-8	-14±-2.7			50
Lomnitz	N/A	N/A	N/A			N/A
Lomnitz and Linear	N/A	N/A	N/A	N/A		N/A
GRL	N/A	N/A	N/A	N/A		N/A
Exponential and Linear	N/A	N/A	N/A	N/A		N/A
Modified Omori	N/A	N/A	N/A	N/A		N/A
Power	N/A	N/A	N/A			N/A
Power and Linear	-2.1±0.23	50±-22	-3.3E13±1.4E13	-0.23±21		11
Burgers	N/A	N/A	N/A	N/A	N/A	N/A
Modified Omori and Linear	N/A	N/A	N/A	N/A	N/A	N/A
GRL and Linear	N/A	N/A	N/A	N/A	N/A	N/

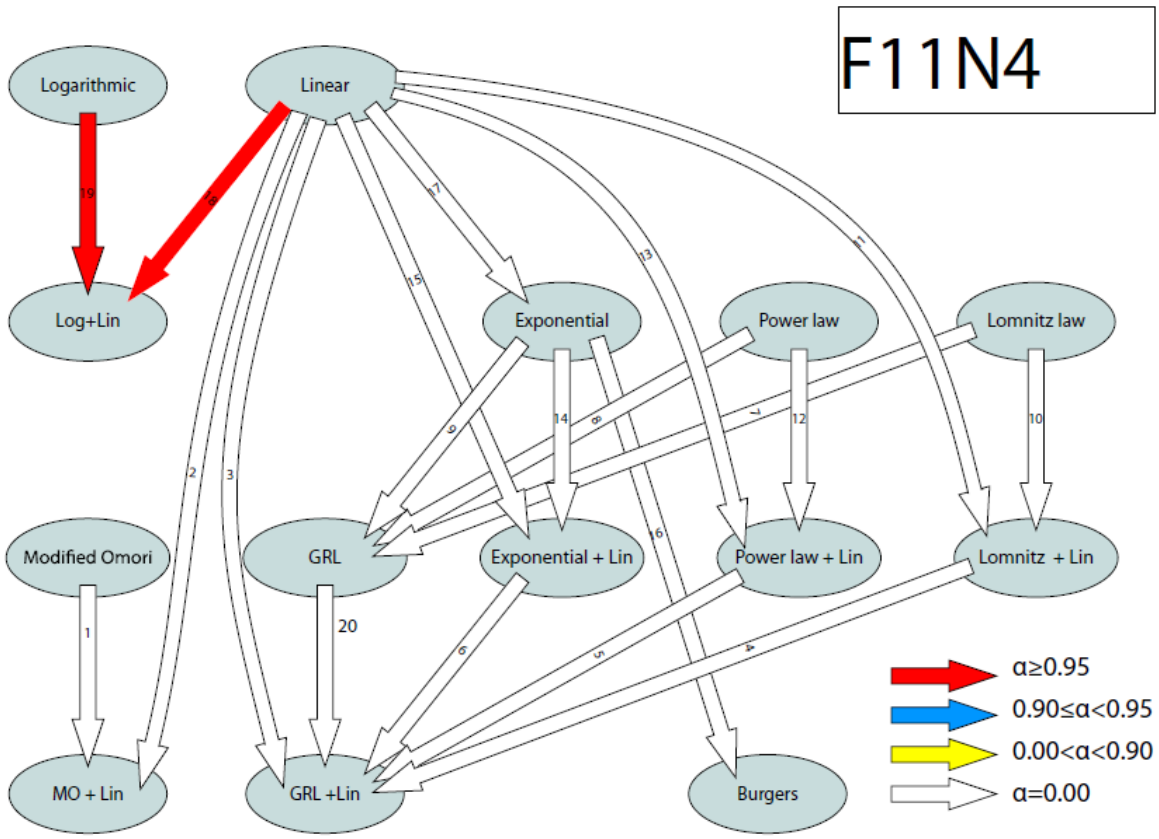

Figure C8: Hierarchy corresponding to Table C8.

Table C9: Parameter and χ^2 values for the M10N1 synthetic time-series. It was created with similar total displacement amplitude to MENT of the Denali network and produced from the Lomnitz relation. "N/A" here means that no reasonable fit was able to be obtained. The noise level is zero.

Function	Parameter 1	Parameter 2	Parameter 3	Parameter 4	Parameter 5	χ^2
Linear	34±0.051	101±0.087				1.0E3
Logarithmic	120±0.045	39±0.032				220
Logarithmic and Linear	97±0.15	29±0.063	33±0.17			45
Exponential	2.3±0.097	150±0.16	1.9±0.0052			49
Lomnitz	-11±0.18	58±0.14	10.4±0.088			1.0E-3
Lomnitz and Linear	-12±0.23	58±0.52	11±0.19	0.52±0.51		0.010
GRL	-11±0.26	590±7.9	0.10±0.0028	0.019±0.0093		0.028
Exponential and Linear	-5.1±0.13	93±0.29	3.9±0.023	43±0.28		4.7
Modified Omori	-11±0.25	1.5E3±300	8.9±0.31	1.0±0.010		0.098
Power	5.7±0.13	430±1.6	0.20±0.001			5.8
Power and Linear	-9.5±0.19	510±3.6	0.14±0.0017	17±0.44		0.27
Burgers	-9.1±0.21	50±0.75	7.2±0.14	150±0.53	0.93±0.017	0.15
Modified Omori and Linear	-11±0.32	380±92	6.9±0.72	1.2±0.067	8.4±2.4	0.091
GRL and Linear	-11±0.33	550±14	0.12±0.0057	0.17±0.045	8.8±2.4	0.068

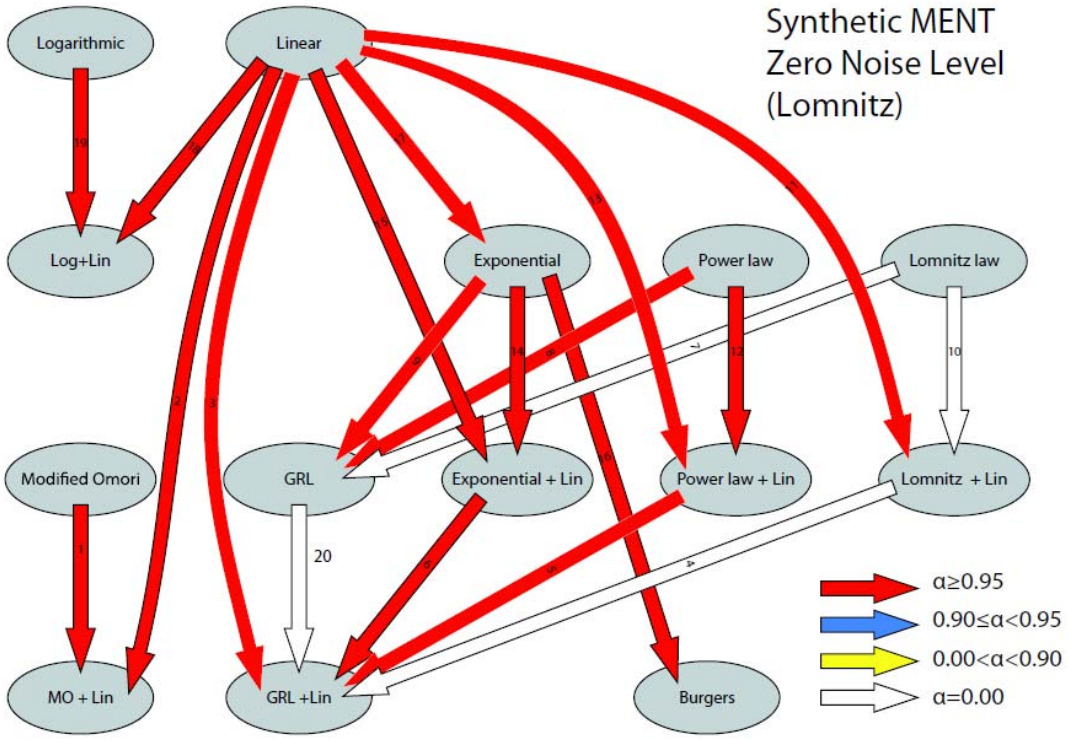

Figure C9: Corresponding hierarchy for Table C9.

Table C10: Parameter and χ^2 values for the M10N2 synthetic time-series. It was created with similar total displacement amplitude to MENT of the Denali network and produced from the Lomnitz relation. "N/A" here means that no reasonable fit was able to be obtained. The noise level is normal noise and random walk.

Function	Parameter 1	Parameter 2	Parameter 3	Parameter 4	Parameter 5	χ^2
Linear	24±0.081	93±0.14				200
Logarithmic	110±0.074	34±0.048				120
Logarithmic and Linear	74±0.23	22±0.094	40.2±0.26			32
Exponential	1.7±0.14	150±0.34	1.5±0.0074			19
Lomnitz	-5.0±0.20	65±0.32	5.4±0.068			17
Lomnitz and Linear	-3.7±0.24	78±2.0	4.2±0.14	-8.9±1.3		17
GRL	-4.4±0.27	340±5.8	0.21±0.0089	0.052±0.024		17
Exponential and Linear	16±0.11	8.2E-5±0.0020	-6.3±15	120±0.33		282
Modified Omori	-4.6±0.28	2.1E3±1.4E3	4.9±0.33	1.0±0.025		18
Power	-2.2±0.16	290±1.6	0.32±0.0028			17
Power and Linear	-2.7±0.21	290±2.2	0.29±0.0079	4.5±1.2		17
Burgers	-19±1.1	30±1.0	26±1.2	150±0.47	1.2±0.011	13
Modified Omori and Linear	-3.7±0.36	8.4E3±1.8E05	4.2±1.2	1.0±0.21	-8.5±11	17
GRL and Linear	-11±9.3	1.3E3±2E4	8.2E-3±0.044	-3.6±0.95	-210±55	15

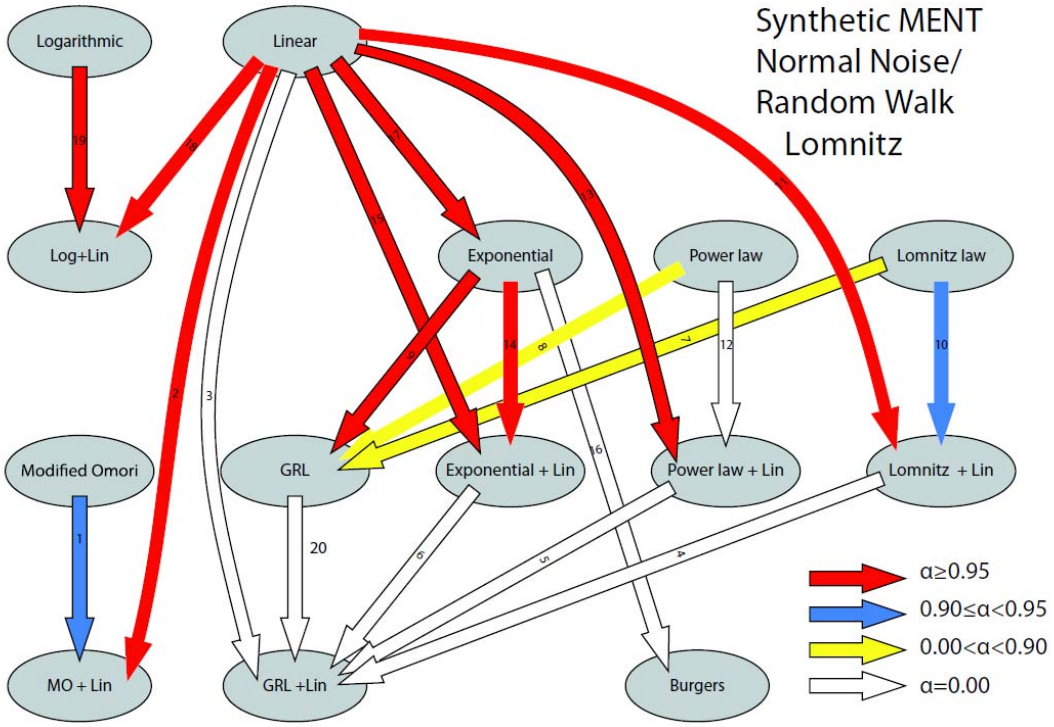

Figure C10: Corresponding hierarchy for Table C10.

Table C11: Parameter and χ^2 values for the M10N3 synthetic time-series. It was created with similar total displacement amplitude to MENT of the Denali network and produced from the Lomnitz relation. "N/A" here means that no reasonable fit was able to be obtained. The noise level is random walk only.

Function	Parameter 1	Parameter 2	Parameter 3	Parameter 4	Parameter 5	χ^2
Linear	36±0.051	99±0.087				1.1E3
Logarithmic	130±0.045	38±0.032				330
Logarithmic and Linear	97±0.15	28±0.063	34±0.17			150
Exponential	5.1±0.097	150±0.16	1.9±0.0052			140
Lomnitz	-7.5±0.17	59±0.14	9.8±0.082			98
Lomnitz and Linear	-6.7±0.21	62±0.59	8.9±0.16	-3.3±0.55		98
GRL	-6.2±0.23	530±6.2	0.12±0.0030	0.076±0.0097		98
Exponential and Linear	-1.8±0.13	93±0.31	3.7±0.023	42±0.29		99
Modified Omori	-6.2±0.23	850±98	7.4±0.26	1.1±0.011		98
Power	-2.4±0.13	420±1.6	0.21±0.0011			101
Power and Linear	-5.2±0.18	470±3.2	0.15±0.0019	14.5±0.46		98
Burgers	-3.7±0.19	60±1.3	5.4±0.12	150±1.2	0.71±0.027	97
Modified Omori and Linear	-4.3±0.24	140±8.0	2.5±0.27	2.2±0.17	24±1.7	98
GRL and Linear	-4.3±0.24	430±7.5	0.18±0.0057	0.54±0.035	25±1.7	98

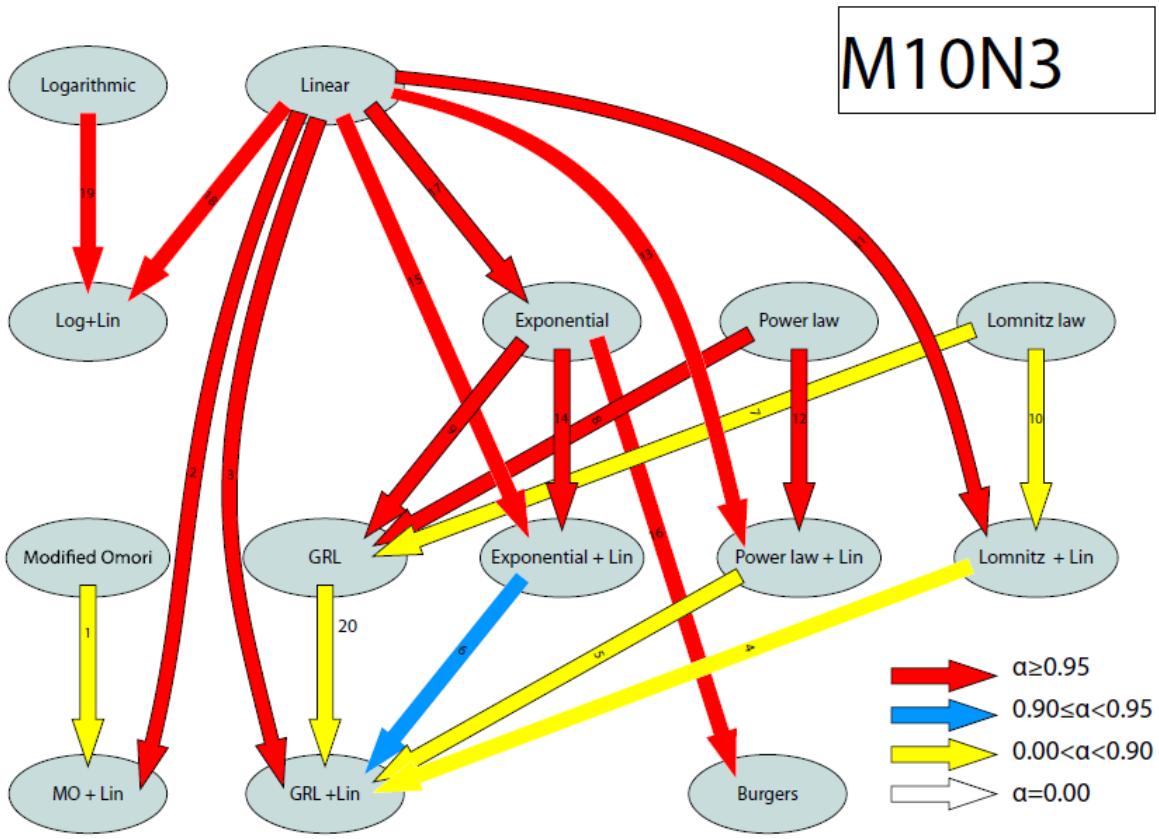

Figure C11: Corresponding hierarchy for Table C11.

Table C12: Parameter and χ^2 values for the M10N4 synthetic time-series. It was created with similar total displacement amplitude to MENT of the Denali network and produced from the Lomnitz relation. "N/A" here means that no reasonable fit was able to be obtained. The noise level is normal noise only.

Function	Parameter 1	Parameter 2	Parameter 3	Parameter 4	Parameter 5	χ^2
Linear	36±0.21	94±0.35				76
Logarithmic	120±0.19	38±0.13				11
Logarithmic and Linear	110±0.60	34±0.25	14±0.69			9.3
Exponential	-5.3±0.41	140±0.51	2.6±0.025			2.0
Lomnitz	-22±0.98	49±0.44	20.0±0.87			4.7
Lomnitz and Linear	-9.9±0.66	110±4.2	5.1±0.28	-55±3.0		2.1
GRL	-7.5±0.58	410±8.8	0.3±0.013	0.80±0.031		1.9
Exponential and Linear	-6.9±0.48	130±1.9	3.0±0.068	12±1.5		1.8
Modified Omori	-7.5±0.58	160±2.2	0.66±0.13	5.0±0.76		1.9
Power	-14±0.6	590±10.3	0.13±0.0027			2.9
Power and Linear	-9.2±0.6	490±8.0	0.23±0.010	-29±2.5		2.0
Burgers	-6.9±0.0	130±0.0	3.0±0.0	4.3E6±0.0	2.1E-6±0.0	2.7
Modified Omori and Linear	-6.9±0.64	130±8.6	7.9E-7±0.27	3.8E06±1.3E12	12±4.5	1.8
GRL and Linear	-5.9±0.62	360±12	0.38±0.023	1.2±0.075	19±2.6	1.8

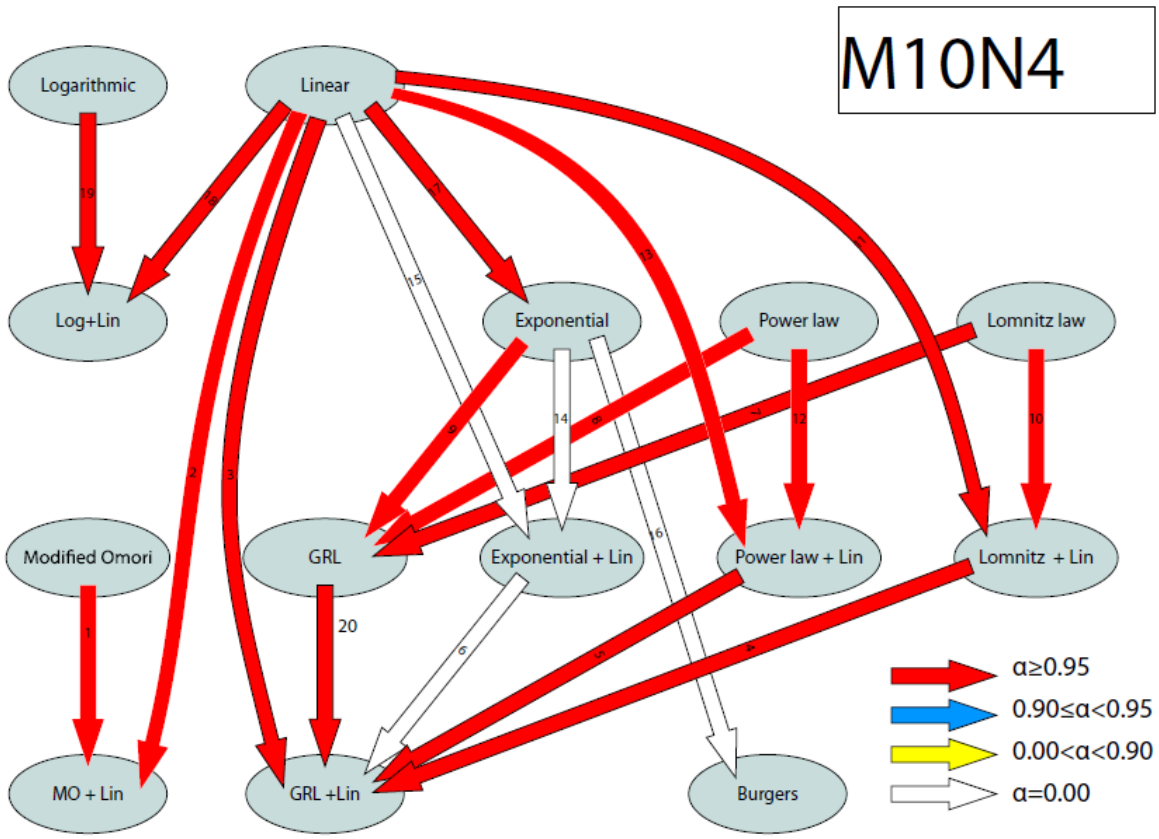

Figure C12: Corresponding hierarchy for Table C12.

Table C13: Parameter and χ^2 values for the M11N4 synthetic time-series. It was created with similar total displacement amplitude to MENT of the Denali network and produced from the Exponential relation. "N/A" here means that no reasonable fit was able to be obtained. The noise level is normal noise.

Function	Parameter 1	Parameter 2	Parameter 3	Parameter 4	Parameter 5	χ^2
Linear	23±0.10	87±0.17				230
Logarithmic	100±0.093	33±0.06				81
Logarithmic and Linear	84±0.29	27±0.12	23±0.33			59
Exponential	-9.4±0.18	130±0.27	2.2±0.012			15
Lomnitz	-18±0.33	51±0.27	11±0.19			30
Lomnitz and Linear	-10.2±0.25	160±4.8	2.5±0.081	-76.7±2.5		16
GRL	-9.3±0.23	290±2.6	0.47±0.0098	1.0±0.018		14
Exponential and Linear	-9.7±0.22	130±1.7	2.3±0.035	2.7±1.1		15
Modified Omori	-9.4±0.2	130±0.47	3.5E-7±0.021	6.3E6±3.8E11		15
Power	23±0.10	87±0.17	4.2E13±2.3E12			232
Power and Linear	N/A	N/A	N/A	N/A	N/A	N/A
Burgers	-9.7±0.21	129±0.0	2.3±0.0	1.9E7±0.0	1.5E-7±0.0	15
Modified Omori and Linear	-9.7±0.22	130±1.6	1.5E7±0	1.5E7±0.0	2.9±1.1	15
GRL and Linear	-8.3±0.26	250±6.1	0.54±0.017	1.4±0.060	20.0±3.0	0.03

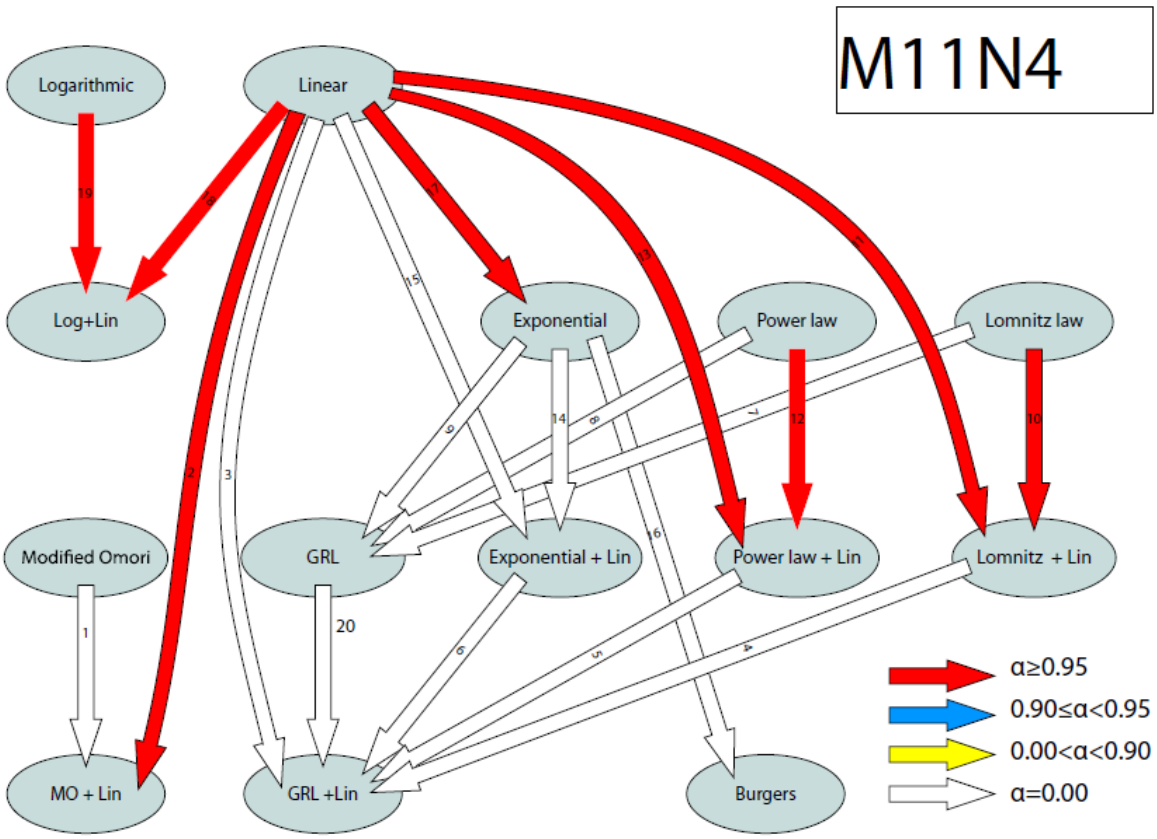

Figure C13: Corresponding hierarchy for Table C13.

Table C14: Parameter and χ^2 values for the M11N3 synthetic time-series. It was created with similar total displacement amplitude to MENT of the Denali network and produced from the Exponential relation. "N/A" here means that no reasonable fit was able to be obtained. The noise level is random walk only.

Function	Parameter 1	Parameter 2	Parameter 3	Parameter 4	Parameter 5	χ^2
Linear	31±0.051	110±0.087				1.6E3
Logarithmic	130±0.045	43±0.032				520
Logarithmic and Linear	100±0.15	33±0.062	34±0.17			330
Exponential	-7.4±0.099	170±0.15	2.0±0.0047			90
Lomnitz	-18±0.17	68±0.15	9.2±0.068			160
Lomnitz and Linear	-8.5±0.13	210±2.7	2.2±0.030	-99±1.4		90
GRL	-7.2±0.12	340±1.2	0.51±0.0043	1.0±0.0078		90
Exponential and Linear	4.5±0.096	2.3E7±2.2E8	2.7E-3±0.014	6.3E4±3.1E5		192
Modified Omori	-7.5±0.092	170±0.0	4.6E-7±0.0	4.5E6±0.0		90
Power	-14±0.13	480±1.6	0.21±9.1E-4			120
Power and Linear	-8.2±0.13	430±0.80	0.46±5.2E-3	-64±1.1		88
Burgers	-7.3±0.11	170±1.0	2.0±0.014	1.8E7±0.0	-7.9E-8±0.0	89
Modified Omori and Linear	-7.3±0.11	170±3.0	1.1E-6±0.029	1.9E6±0.029	1.6±1.3	89
GRL and Linear	N/A	N/A	N/A	N/A	N/A	N/A

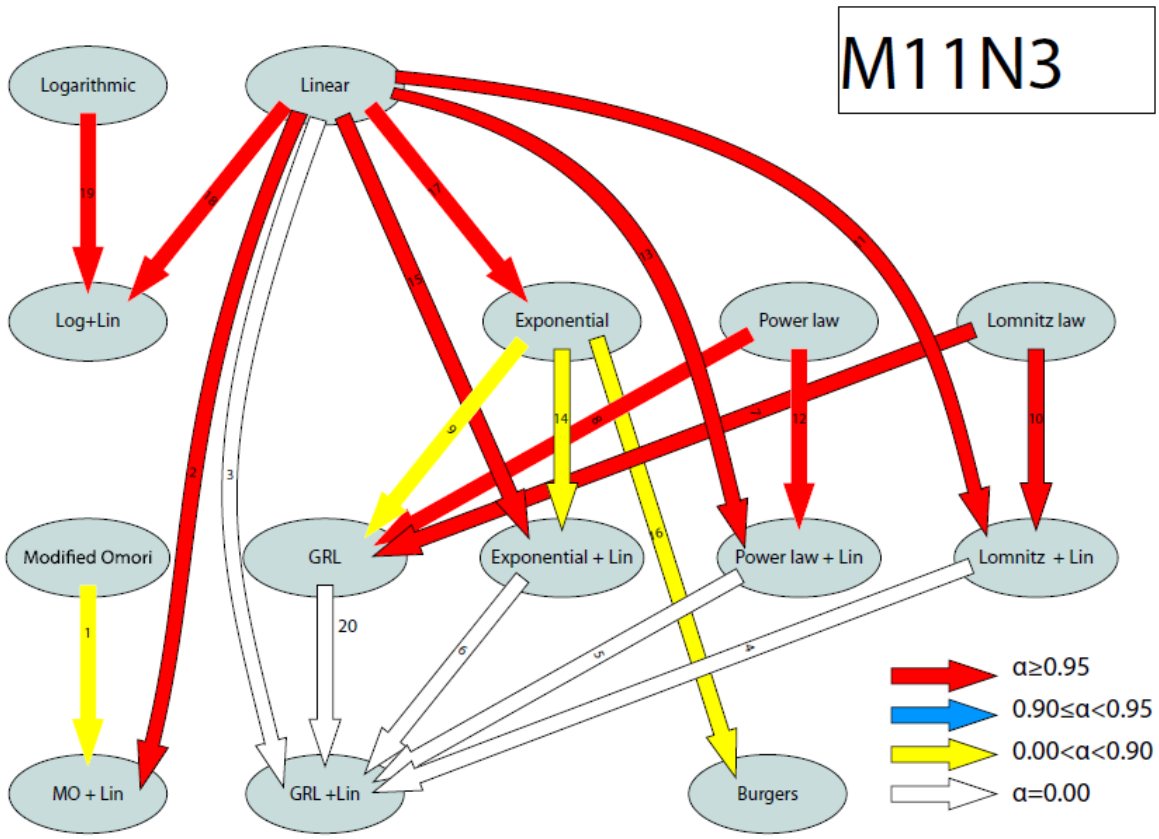

Figure C14: Corresponding hierarchy for Table C14.

Table C15: Parameter and χ^2 values for the M11N2 synthetic time-series. It was created with similar total displacement amplitude to MENT of the Denali network and produced from the Exponential relation. "N/A" here means that no reasonable fit was able to be obtained. The noise is random walk and normal.

Function	Parameter 1	Parameter 2	Parameter 3	Parameter 4	Parameter 5	χ^2
Linear	27±0.047	98±0.077				1100
Logarithmic	120±0.043	38±0.027				320
Logarithmic and Linear	98±0.13	31±0.053	24±0.15			216
Exponential	-8.3±0.084	150±0.13	2.1±0.0047			34
Lomnitz	-18±0.15	57±0.13	11±0.087			90
Lomnitz and Linear	-8.5±0.11	220±2.9	2.1±0.028	-105±1.3		32
GRL	-7.1±0.098	310±1.0	0.55±0.044	1.2±0.0075		34
Exponential and Linear	-7.3±0.094	170±1.2	1.8±0.013	-13±0.68		34
Modified Omori	-8.3±0.20	150±0.99	1.2E-7±0.045	1.6E7±0.045	1.6E7±6.0E12	34
Power	-14±0.11	470±1.6	0.18±8.0E-4			61
Power and Linear	-8.1±0.11	404±0.65	0.51±0.0059	-75.8±1.2		33
Burgers	-7.1±0.13	210±93	1.7±0.26	-86±58	0.57±0.85	34
Modified Omori and Linear	-8.2±0.16	940±670	1.5±0.31	1.3±0.25	-86±15	33
GRL and Linear	-8.5±0.17	490±30.7	0.51±0.0085	-0.42±0.26	-150±27	33

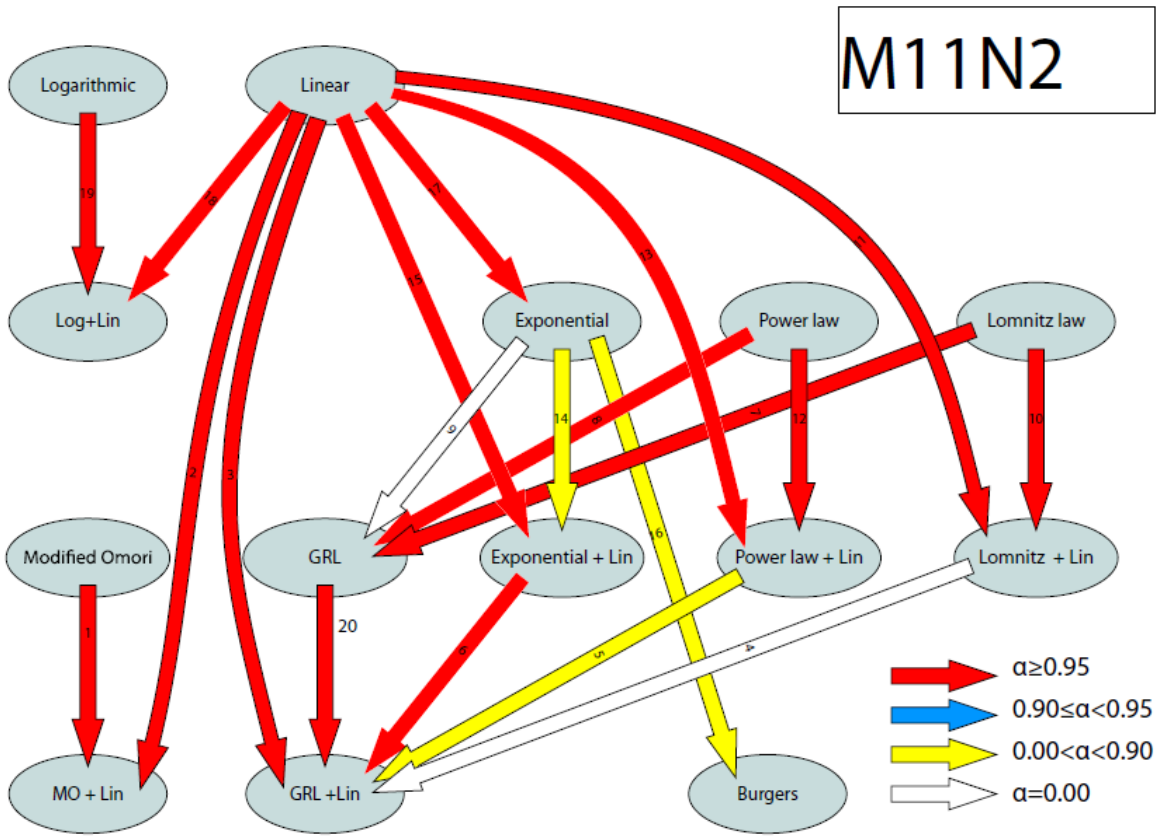

Figure C15: Corresponding hierarchy for Table C15.

Table C16: Parameter and χ^2 values for the M11N1 synthetic time-series. It was created with similar total displacement amplitude to MENT of the Denali network and produced from the Exponential relation. "N/A" here means that no reasonable fit was able to be obtained. There is zero noise here.

Function	Parameter 1	Parameter 2	Parameter 3	Parameter 4	Parameter 5	χ^2
Linear	31±0.051	110±0.087				1500
Logarithmic	130±0.045	43±0.032				440
Logarithmic and Linear	100±0.15	32±0.062	36±0.17			230
Exponential	-6.9±0.098	170±0.15	2.0±4.6E-3			0.0045
Lomnitz	-17±0.16	69±0.15	8.8±0.063			61
Lomnitz and Linear	-8.2±0.13	210±2.8	2.2±0.030	-95.4±		0.56
GRL	-6.9±0.12	340±1.3	0.50±0.044	1.0±0.0081		0.016
Exponential and Linear	-7.0±0.11	170±1.1	2.0±0.014	1.3±0.65		0.040
Modified Omori	-7.3±0.12	170±0.54	0.074±0.018	28±6.4		0.098
Power	-13±0.13	47±1.6	0.21±9.3E-3			28
Power and Linear	-7.9±0.13	420±0.80	0.46±0.0052	-62±1.1		0.34
Burgers	-6.9±0.15	170±17	2±0.11	21±4.5E5	0.0046±98	0.025
Modified Omori and Linear	-7.3±0.16	230±23	0.46±0.15	4.5±1.4	19±6.3	0.087
GRL and Linear	-6.6±0.15	320±4.8	0.52±0.0072	1.1±0.041	11±2.9	0.093

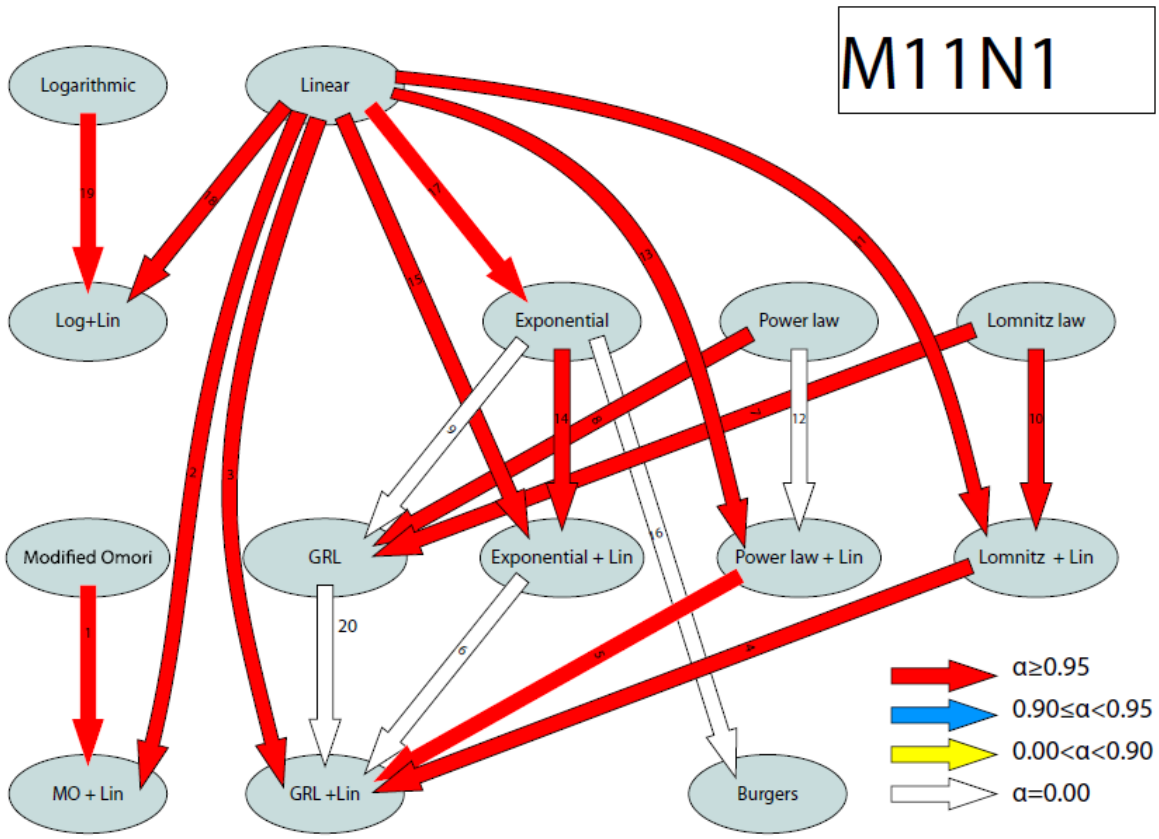

Figure C16: Corresponding hierarchy for Table C16.

VIII. Bibliography

Bürgman, R., and G. Dresen (2008). Rheology of the Lower Crust and Upper Mantle: Evidence from Rock Mechanics, Geodesy, and Field Observations, Annual Review of Earth and Planetary Sciences, 36, 531-67.

Eberhart-Phillips, D., et al. (2003), The 2002 Denali Fault earthquake, Alaska: a large magnitude, slip-partitioning event, Science, 300, 1113–1118.

Hetland, E. A., and B. H. Hager (2006), The effects of rheological layering on post-seismic deformation, Geophysical Journal International, 166, 277, doi:10.1111/j.1365-246X.2006.02974.x.

Freed, A.M., R. Bürgmann, E. Calais, and J. Freymuller (2006a), Implications of deformation following the 2002 Denali, Alaska, earthquake for postseismic relaxation processes and lithospheric rheology, Journal of Geophysical Research, 111, B01401, doi:10.1029/2005JB003894.

Freed, A.M., R. Bürgmann, E. Calais, and J. Freymuller, and S. Hreinsdôttir (2006b), Stress-dependent power law flow in the upper mantle following the 2002, Denali, Alaska, earthquake. Earth and Planetary Science Letters, 252, 481-489.

Freed, A. M. (2007), Afterslip (and only afterslip) following the 2004 Parkfield, California, earthquake, Geophysical Research Letters, 34, L06312, doi:10.1029/2006GL029155.

Helmstetter, Angès and Bruce E. Shaw (2008), Afterslip and Aftershocks in the rate and state friction law, Journal of Geophysical Research, 0148-0227.

Johnson, K., R. Bürgmann, and K. Larson, 2006, Frictional Properties on the San Andreas Fault near Parkfield, California, Inferred from Models of Afterslip following the 2004 Earthquake. Bulletin of the Seismological Society of America, 96, S321-S338, doi:10.1785/0120050808.

Johnson, K., R. Bürgmann, and J. Freymuller, 2009, Coupled afterslip and viscoelastic flow following the 2002 Denali Fault, Alaska earthquake, Geophysical Journal International, 176, 670-682, doi:10.1111/j.1365-246X.2008.04029.x

Langbein, J., J. R. Murray, and H. A. Snyder (2006), Coseismic and initial postseismic deformation from the 2004 Parkfield, California, earthquake, observed by Global Positioning System, electronic distance meter, creepmeters, and borehole strainmeters, Bulletin of the Seismological Society of America, 96, S304–S320, doi:10.1785/0120050823

Marone, C., C. H. Scholz, and R. Bilham (1991), On the mechanics of earthquake afterslip, Journal of Geophysical Research, 96, 8441–8452

Montesi, L. G. J. (2004), Controls of shear zone rheology and tectonic loading on postseismic creep, Journal of Geophysical Research, 109, B10404, doi:10.1029/2003JB002925.

Peltzer, G., P. Rosen, F. Rogez, and K. Hudnut (1998), Poroelastic rebound along the 1992 Landers earthquake surface rupture, Journal of Geophysical Research, 103, 30, 131-30,145.

Perfettini, H., and J.-P. Avouac (2004), Postseismic relaxation driven by brittle creep: A possible mechanism to reconcilegeodetic measurements and the decay rate of aftershocks, application to the Chi-Chi earthquake, Taiwan, Journal of Geophysical Research, 109, B02304, doi:10.1029/2003JB002488.

Savage, J. C., J. L. Svarc, and S.-B. Yu (2005), Postseismic relaxation and transient creep, Journal of Geophysical Research,110, B11402, doi:10.1029/2005JB003687.

Savage, J. C. (2007), Postseismic relaxation associated with transient creep rheology, Journal of Geophysical Research, 112, B05412, doi:10.1029/2006JB004688.

Savage, J. C., and J. Langbein (2008), Postearthquake relaxation after the 2004 M6 Parkfield, California, earthquake andrate-and-state friction, Journal of Geophysical Research, 113, B10407, doi:10.1029/2008JB005723.